CRYSTAL GROWTH & DESIGN

Article

Cite This: Cryst. Growth Des. 2018, 18, 3805−3819

pubs.acs.org/crystal

Structural Modularity of Unique Multicomponent Hydrogen-Bonded Organic Frameworks Based on Organosilanetriols and Silanediols as Molecular Building Blocks

Miriam de J. Velásquez-Hernández,[†] Aaron Torres-Huerta,[†] Diego Martínez-Otero,[†] Elí Sánchez-González,[§] Uvaldo Hernández-Balderas,[†] Ilich A. Ibarra,[§] and Vojtech Jancik*[,†]

[†]Centro Conjunto de Investigación en Química Sustentable UAEM-UNAM, Carretera Toluca-Atlacomulco, km.14.5, 50200, México

[§]Laboratorio de Fisicoquímica y Reactividad de Superficies (LaFReS), Instituto de Investigaciones en Materiales, Universidad Nacional Autónoma de México, Circuito Exterior s/n, CU, Del. Coyoacán, 04510, Ciudad de México, México

Supporting Information

ABSTRACT: In this study we examined the use of a new class of molecular building blocks with tetrahedral nodes based on organo-bis(silanetriols) (1,4-$[(HO)_3SiOCEt_2]_2C_6H_4$ (**1**) and 4,4′-$[(HO)_3SiOCEt_2]_2$-(1,1′-biphenyl) (**2**)) and organo-bis(silanediol) (1,4-$[\{(HO)_2(^tBuO)Si\}OCEt_2]_2C_6H_4$ (**3**)) for the synthesis of multicomponent hydrogen-bonded organic frameworks (HOFs) with adjustable supramolecular patterns, and modular assembly. Thus, such reticular arrangements were readily obtained by the cocrystallization of bridged organosilanols (**1**, **2**, and **3**) with an organic diamine (1,4-diazabicyclo[2.2.2]octane (**a**) or *trans*-1,2-bis(4-pyridyl)-ethylene (**b**)) to yield the corresponding HOFs **1a**, **1b**, **2a**, **2b**, **3a**, and **3b**. Single-crystal X-ray diffraction analysis revealed that the dimensionality of the network, and by consequence, its porosity, can be easily engineered by means of the modulation of the central organic backbone of the organosilanol-based tectons, as well as by the Lewis basicity and the size of the corresponding organic diamine. In this context, it was found that although **1a** presents a nonporous arrangement, changing either the organic diamine as in **1b**, or the spacer's size as in **2a**, it is possible to generate one-dimensional channels or zero-dimensional voids, respectively. Moreover, through gas sorption experiments, it was demonstrated that **1b** exhibits structural flexibility and permanent porosity with selective adsorption of CO_2 over N_2.

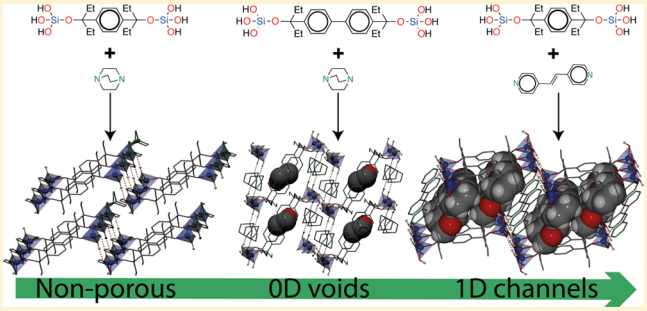

INTRODUCTION

Hydrogen-bonded organic frameworks (HOFs) are a new class of porous crystalline materials constructed from molecular building blocks, which are assembled by intermolecular hydrogen-bonding interactions. To date, the HOFs have been used in a wide range of practical applications such as gas storage and separation,[1−6] sensing,[7] semiconductors,[8] and proton conductions.[9,10] In comparison to other kinds of reticular porous materials comprised by molecular subunits, such as metal−organic frameworks (MOFs) and covalent-organic frameworks (COFs), HOFs can be obtained under mild reaction conditions, and they can be readily regenerated by recrystallization.[11] Additionally, they present low density and low toxicity, as they are mainly composed of light elements (C, H, O, N, B, etc.).

The HOFs can be either single-component or multicomponent, where the former are more restricted regarding molecular design and functionality.[11] By contrast, multicomponent HOFs are much more versatile, as they are comprised of at least two different types of molecular constituents with adjustable functionality. Moreover, the multicomponent HOFs can be prepared under milder reaction conditions, as their synthesis is based on the fundamental principles of molecular recognition between complementary hydrogen-bond donating/accepting functional groups.[12−14] Consequently, this synthetic approach takes advantage of crystal engineering principles to achieve controlled assembly.[15] Nevertheless, the accurate prediction of the properties and structural arrangement of the resultant reticular network is still a very challenging task. Thus, the primary goal of crystal engineering is to modulate the intermolecular interactions to control the organization of molecules within the supramolecular arrangement. To achieve this structural modularity is particularly essential in the design of porous materials and requires a profound understanding of the factors that affect the self-recognition between the molecular tectons.[16] In this regard, carboxylic and boronic acid groups figure among the most-investigated hydrogen-bond functionalities for the synthesis of

Received: January 7, 2018
Revised: May 17, 2018
Published: June 4, 2018

DOI: 10.1021/acs.cgd.8b00030
Cryst. Growth Des. 2018, 18, 3805−3819

supramolecular hydrogen-bonded networks, and it has been shown that in those systems the most common interaction is the self-association leading to the formation of the homodimeric eight-membered ring, which can be described in terms of graph-set analysis by the $R_2^2(8)$ motif (Scheme 1a).[17−32] It is noteworthy that although both of them exhibit the formation of this robust $R_2^2(8)$ synthon,[17,18] in the case of boronic acid the additional OH group attached to the boron atom can bind to other molecules by hydrogen-bonding interactions. Additionally, this feature also permits the boronic acid moieties to adopt different conformations such as *syn-syn*, *syn-anti*, and *anti-anti*, which enriches the supramolecular arrangement due to conformational flexibility (Scheme 1b).[21−24,33] More recently, organosulfonic and organophosphonic acid derivatives have been explored as molecular building blocks. Because of the tridentate character, and the tetrahedral geometry of the SO_3H and PO_3H_2 moieties, supramolecular assemblies with interesting topologies and structural diversity can be generated (Scheme 1c).[34−50] However, the high polarity of the organosulfonic and organophosphonic acid derivatives limits considerably their solubility in organic solvents, and therefore, sulfonic acids are usually handled as sodium salts.[35] Consequently, due to these facts the wider use of such compounds as molecular building blocks has been hampered.

Scheme 1. (a) Homodimeric $R_2^2(8)$ Synthon Obtained by the Self-Association of Carboxylic or Boronic Acid Moieties, (b) Conformations of the Boronic Acid Moiety, and (c) Isoelectronic Tetrahedral Tectons

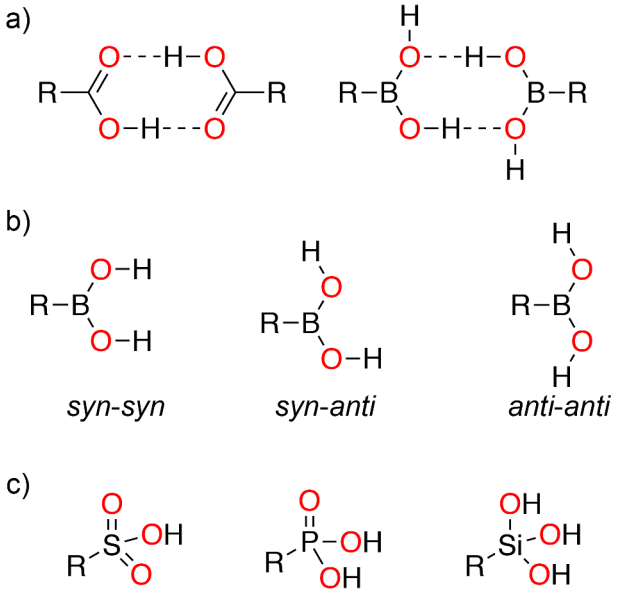

As an alternative, we proposed the use of organo-bis(silanetriols) as molecular tectons, because they are isoelectronic with the corresponding organophosphonic and organosulfonic acid derivatives. Additionally, they also share the same tetrahedral geometry around the central atom. Nonetheless, the organosilanetriols present some advantages over organophosphonic and organosulfonic acid derivatives. First, organosilanetriols are much less acidic and less polar; hence, they present higher solubility in organic solvents and remain neutral under the reaction conditions. Second, they contain three OH groups attached to the silicon center, which improves their hydrogen-bonding capabilities.

Notwithstanding the versatility of organosilanetriols, their extended use as molecular building blocks to produce crystalline supramolecular arrangements has been limited due to low stability of $Si(OH)_3$ groups toward self-condensation reactions.[51−53] In fact, to prevent the formation of polycondensation byproducts during the synthesis of organo-mono(silanetriols), it is mandatory to use kinetically stabilizing groups such as bulky organic substituents.[51,52,54] Nevertheless, it was also demonstrated that an alternative way to achieve the stabilization of N- and C-bonded organo-mono(silanetriols) consists of the formation of diamin-silanol adducts, where the diamine molecules are trapped between adjacent $Si(OH)_3$ moieties, reducing the kinetic tendency of silanetriols to self-condensation.[55−57] On the other hand, Corriu et al. reported the first synthesis of C-bonded organo-bis(silanetriols), where the Si−C bonds lower the acidity of the Si−OH groups improving the stability of the compounds.[58−60] Nevertheless, these organo-bis(silanetriols) were not characterized by SCXRD analysis, because the presence of more than one $Si(OH)_3$ moiety per molecule enhances the probability of their polymerization via the formation of Si−O−Si bridges after longer periods of time in solution hindering the growth of suitable monocrystals.[58,59] Given all these considerations, our research group reported a sustainable synthetic method for stable organo-mono(silanetriols) and organo-bis(silanetriols) were the silicon atom binds to four oxygen atoms as in silica materials,[61] which enhances the acidity of the OH groups.[60] Moreover, in this work we also showed the first example of a multicomponent hydrogen-bonded supramolecular network (**1a**) obtained by the cocrystallization of bridged organo-bis(silanetriol) (**1**) and 2 equiv of 1,4-diazabicyclo[2.2.2]octane (DABCO) (**a**).[61] Therefore, motivated by the success of this binary assembly method for the construction of novel organo bis(silanetriol)-based extended networks, herein, we report a deeper analysis of the use of bridged organo-bis(silanols) as molecular tectons for the synthesis of such hydrogen-bonded networks, with adjustable supramolecular patterns and modular assembly.

For this purpose selected organo-bis(silanols) 1,4-$[(HO)_3SiOCEt_2]_2C_6H_4$ (**1**), 4,4′-$[(HO)_3SiOCEt_2]_2$-(1,1′-biphenyl) (**2**), and 1,4-$[\{(HO)_2(^tBuO)Si\}OCEt_2]_2C_6H_4$ (**3**) were co-crystallized with DABCO (**a**) and *trans*-1,2-bis(4-pyridyl)-ethylene (4,4′-bpe) (**b**), and in order to gain a better understanding of the factors that determine the structural arrangement, (i) the basicity of the organic amines (ii) the size of the organic bridging group within the organosilanol-based tectons and (iii) the number of OH groups attached to silicon center were systematically modified. This leads to the formation of five new HOFs: $\{(1,4\text{-}[(HO)_3SiOCEt_2]_2C_6H_4)\cdot(4,4'\text{-bpe})\}\cdot 4THF$ (**1b**·4THF), $\{(4,4'\text{-}[(HO)_3SiOCEt_2]_2\text{-}(1,1'\text{-biphenyl}))\cdot 2(DABCO)\}\cdot THF$ (**2a**·THF), $\{(4,4'\text{-}[(HO)_3SiOCEt_2]_2\text{-}(1,1'\text{-biphenyl}))\cdot 2(4,4'\text{-bpe})\}\cdot THF$ (**2b**·THF), $\{(1,4\text{-}[\{(HO)_2(^tBuO)Si\}OCEt_2]_2C_6H_4)\cdot 2(DABCO)\}\cdot 2THF$ (**3a**·2THF), and $\{(1,4\text{-}[\{(HO)_2(^tBuO)Si\}OCEt_2]_2C_6H_4)\cdot(4,4'\text{-bpe})\}$ (**3b**). For the sake of clarity, the solvent content in the compound numbers will be, with the exception of Table 1, omitted in the following discussion. The single-crystal X-ray diffraction analysis of these materials reveals that their supramolecular arrangement and porosity can be easily controlled by the modulation of the central backbones of the organosilanol-based tectons and the Lewis basicity of the organic diamine.

DOI: 10.1021/acs.cgd.8b00030
Cryst. Growth Des. 2018, 18, 3805−3819

Table 1. Crystallographic Data for the HOFs 1a, 1b·4THF, 2a·THF, 2b·THF, 3a·2THF, and 3b

	1a[61]	1b·4THF	2a·THF	2b·THF	3a·2THF	3b
empirical formula	$C_{28}H_{54}N_4O_8Si_2$	$C_{44}H_{72}N_2O_{12}Si_2$	$C_{38}H_{66}N_4O_9Si_2$	$C_{50}H_{62}N_4O_9Si_2$	$C_{44}H_{86}N_4O_{10}Si_2$	$C_{36}H_{56}N_2O_8Si_2$
fw (g/mol)	630.93	877.21	779.12	919.21	887.34	701.00
space group	$P\bar{1}$	$P\bar{1}$	$P\bar{1}$	$P\bar{1}$	$P2_1/n$	$P2_1/c$
T (K)	100(2)	100(2)	100(2)	100(2)	100(2)	100(2)
λ (Å)	0.71073	1.54178	1.54178	1.54178	1.54178	0.71073
a (Å)	8.5208(4)	10.0113(4)	9.2526(2)	9.45190(10)	10.5432(4)	11.1858(3)
b (Å)	9.8696(5)	10.5786(4)	9.6010(2)	9.56110(10)	10.0965(4)	9.2167(2)
c (Å)	11.7679(6)	12.8998(4)	13.5651(2)	15.3911(2)	24.1212(9)	18.6477(5)
α (deg)	103.7594(11)	74.9757(19)	81.2971(11)	75.3208(8)	90	90
β (deg)	97.5810(11)	88.026(2)	75.9465(11)	85.8506(7)	90.0303(19)	98.6109(5)
γ (deg)	113.1915(11)	63.2189(19)	66.2153(12)	62.9820(7)	90	90
V (Å^3)	854.90(7)	1172.54(8)	1067.76(4)	1197.18(2)	2567.69(17)	1900.84(8)
crystal size (mm)	0.189 × 0.052 × 0.040	0.247 × 0.202 × 0.104	0.432 × 0.14 × 0.032	0.151 × 0.105 × 0.098	0.238 × 0.210 × 0.177	0.285 × 0.206 × 0.118
Z	1	1	1	1	2	2
$\rho_{calc.}$ (g·cm^{-3})	1.226	1.242	1.212	1.275	1.148	1.225
μ (mm^{-1})	0.154	1.189	1.201	1.161	1.066	0.144
F(000)	342	474	422	490	972	756
θ range for data collection (deg)	1.841 to 26.371	3.564 to 67.734	3.365 to 67.727	2.972 to 70.056	3.665 to 68.240	2.209 to 27.499
no. of reflections	16864	4133	22314	21340	21510	18657
no. of independent reflections (R_{int})	3500 (0.0390)	4133(0.0840)	3788 (0.0346)	4438 (0.0246)	4685 (0.0262)	4334 (0.0240)
no. of data/restraints/parameters	3500/3/201	4133/526/374	3788/71/273	4438/75/327	4685/1086/523	4334/577/333
goodness-on-fit (GOF) on F^2	1.018	1.061	1.043	1.039	1.058	1.075
R_1,[a] wR_2[b] ($I > 2\sigma(I)$)	0.0335, 0.0786	0.0514, 0.1424	0.0403, 0.1042	0.0340, 0.0907	0.0649, 0.1845	0.0368, 0.0996
R_1,[a] wR_2[b] (all data)	0.0436, 0.0844	0.0581, 0.1486	0.0490, 0.1111	0.0384, 0.0942	0.0673, 0.1870	0.0407, 0.1024
largest diff. peak/hole (e·Å^{-3})	0.341, −0.252	0.610, − 0.481	0.508, − 0.216	0.294, − 0.349	0.454, − 0.389	0.391, − 0.318
CCDC	1453231	1815223	1815224	1815225	1815226	1815227

[a] $R_1 = \Sigma||F_o| - |F_c||/\Sigma|F_o|$. [b] $wR_2 = [\Sigma w(F_o^2 - F_c^2)^2/\Sigma w(F_o^2)^2]^{1/2}$.

DOI: 10.1021/acs.cgd.8b00030
Cryst. Growth Des. 2018, 18, 3805−3819

Scheme 2. Synthesis of Multicomponent HOFs Based on Organo-bis(silanols) and Organic Diamines

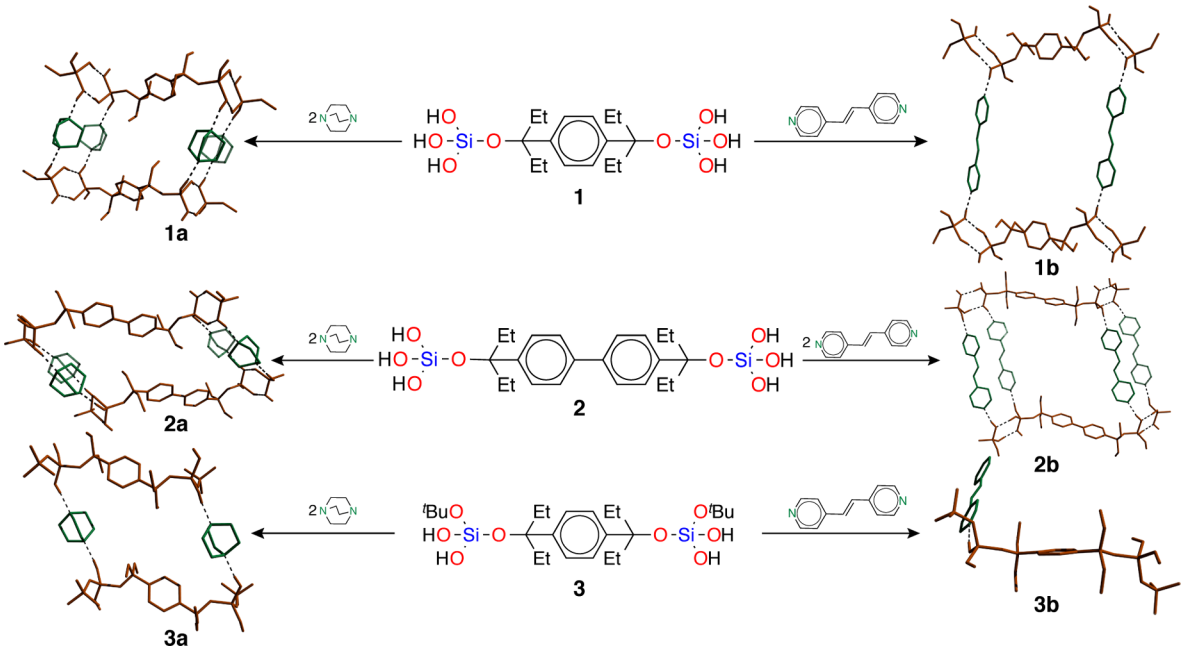

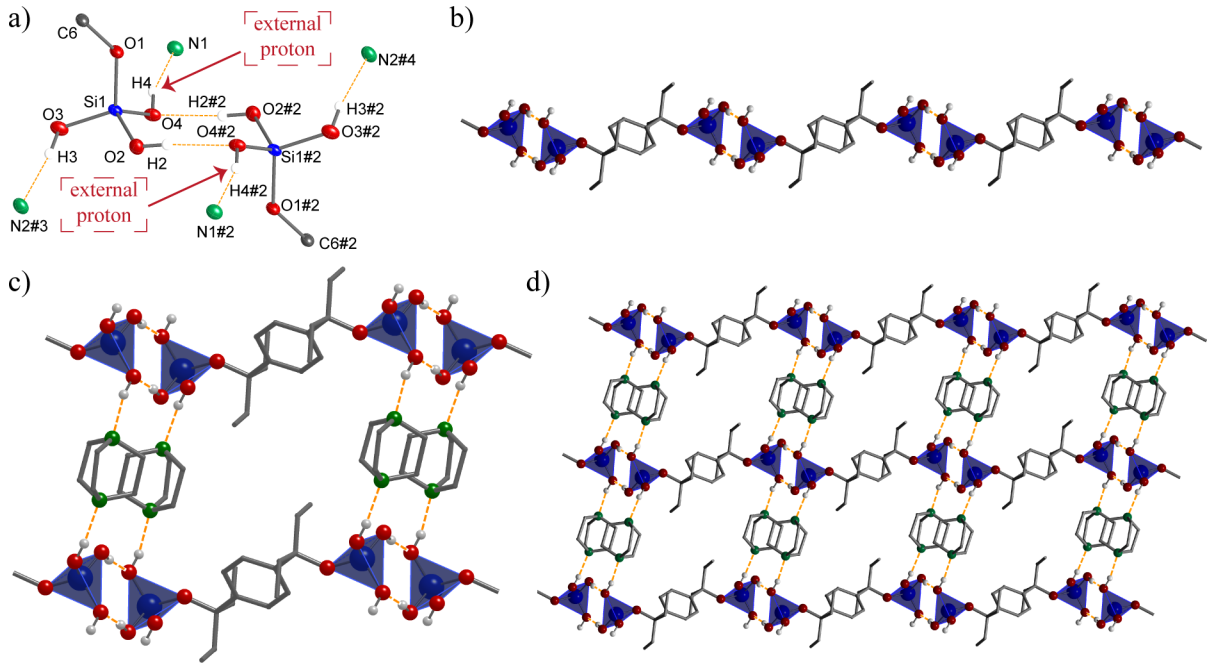

Figure 1. Supramolecular arrangement in HOF **1a**. (a) The $R_2^2(8)$ chair-shaped ring motif. Symmetry codes to generate equivalent positions: #2: $1-x, 1-y, -z$; #3: $x, 1+y, z$; #4: $1-x, -y, -z$. (b) The $C_2^2(26)$ motif. (c) The $R_4^4(36)$ diamine-silanol macrocycle. (d) 2D supramolecular network constructed from the diamine-silanol macrocycles.

RESULTS AND DISCUSSION

The principal aim of this work was to study the use of organo-bis(silanols) as molecular building blocks in the construction of multicomponent hydrogen-bonded supramolecular networks with structural modularity. Consequently, we tested the cocrystallization of the aforementioned organo-bis(silanols) (**1**, **2**, and **3**) in the presence of either DABCO (**a**) or 4,4′-bpe (**b**), to afford the corresponding HOFs (**1a**, **1b**, **2a**, **2b**, **3a**, and **3b**). In all the cases, the organo-bis(silanol) and 2 equiv of the corresponding diamine were dissolved separately in THF, and then such solutions were mixed and stirred for 15 min at room temperature. Afterward, the reaction mixture was concentrated under a vacuum and stored at −24 °C to yield the corresponding HOF as a white crystalline powder. It was observed that **1a**, **2a**, **2b**, and **3a**, have a 2:1 diamine-alkoxysilanol ratio. By contrast, HOFs **1b** and **3b** crystallized with a 1:1 diamine-alkoxysilanol stoichiometric ratio. Furthermore, **1b**, **2a**, **2b**, and **3a** crystallized as THF solvates (Scheme 2). All the compounds were fully characterized by elemental analysis, IR, and single-crystal X-ray diffraction techniques, and the phase purity was analyzed by powder X-ray diffraction (PXRD) patterns (vide infra). Additionally, their

DOI: 10.1021/acs.cgd.8b00030
Cryst. Growth Des. 2018, 18, 3805−3819

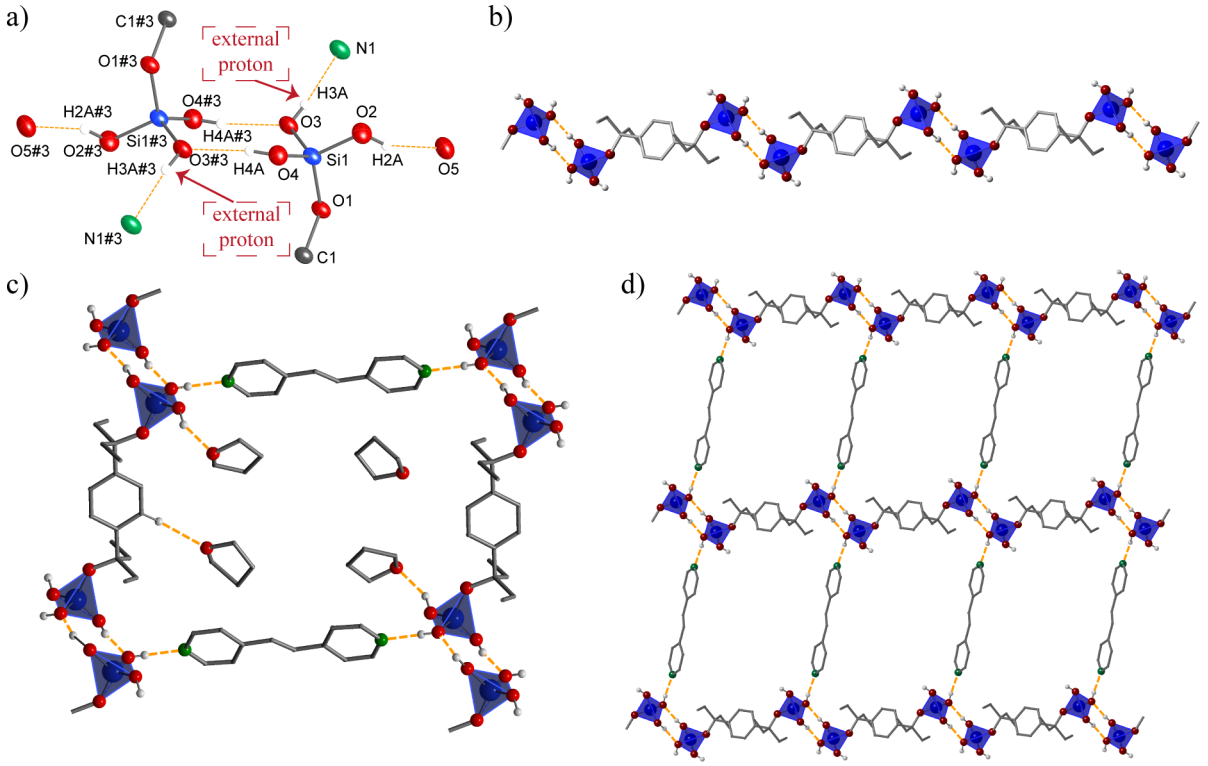

Figure 2. Supramolecular arrangement in HOF **1b**. (a) The $R_2^2(8)$ chair-shaped ring motif. Symmetry codes to generate equivalent positions: #3: 2 − *x*, 1 − *y*, 2 − *z*. (b) The $C_2^2(26)$ motif. (c) The $R_6^6(52)$ diamine-silanol macrocycle. (d) 2D supramolecular network constructed from the diamine-silanol macrocycles.

Table 2. Geometric Parameters for the Hydrogen Bonds in the Crystal Structures of HOFs 1a−3b

HOF	D−H···A	*d*(D···A) (Å)	∠DHA (deg)	symmetry code
1a	O(2)−H(2)···O(4)#2	2.780(2)	173(2)	#2: 1 − *x*,1 − *y*, −*z*
	O(3)−H(3)···N(2)#3	2.742(2)	172(2)	#3: *x*, 1 + *y*, *z*
	O(4)−H(4)···N(1)	2.658(2)	163(2)	
1b	O(2)−H(2A)···O(5)$_{THF}$	2.67(2)	157(3)	#3: 2 − *x*, 1 − *y*, 2 − *z*
	O(3)−H(3A)···N(1)	2.716(2)	174(3)	
	O(4)−H(4A)···O(3)#3	2.703(2)	172(3)	
2a	O(2)−H(2A)···N(1)	2.653(2)	161(2)	#2: *x*, 1 + *y*, *z*
	O(3)−H(3A)···N(2)#2	2.699(2)	177(2)	#3: 1 − *x*, 1 − *y*, −*z*
	O(4)−H(4A)···O(2)#3	2.735(2)	177(2)	
2b	O(2)−H(2)···N(1)	2.705(2)	165(2)	#2: 2 − *x*, −*y*, −*z*
	O(3)−H(3)···O(2)#2	2.736(1)	171(2)	#3: 1 + *x*, −2 + *y*, *z*
	O(4)−H(4)···N(2)#3	2.736(2)	168(2)	
3a	O(3)−H(3A)···N(1)	2.655(2)	167(3)	#2: *x*, −1 + *y*, *z*
	O(4)−H(4A)···N(2)#2	2.672(2)	168(4)	
3b	O(3)−H(3A)···N(1)	2.746(8)	167(2)	#3: 1 − *x*, 0.5 + *y*, 0.5 − *z*
	O(4)−H(4A)···O(3)#3	2.846(1)	163(2)	

thermal stability was studied by thermogravimetric analysis (TGA) under a nitrogen flow. Finally, the permanent porosity and sorption properties of HOF **1b** were also examined.

Single-Crystal X-ray Diffraction Analysis. The HOFs obtained from organo-bis(silanetriols) **1** and **2** (**1a**, **1b**, **2a**, **2b**) crystallized in triclinic $P\bar{1}$ space group, whereas those derived from the organo-bis(silanediol) **3** (**3a** and **3b**) were refined in monoclinic $P2_1/n$ and $P2_1/c$ space groups, respectively (Table 1). In general, the structural analysis of these HOFs shows that the coordination geometry around the silicon atom corresponds to a disordered tetrahedral geometry, which is reflected in the O−Si−O angles ranging from 103.9(3)° to 115.0(1)°, where the Si−O bond lengths lie between 1.601(2) and 1.633(1) Å (see Supporting Information, Table S1). Both of them are within the expected ranges and are comparable with those found in the literature for similar compounds with O−Si bonds.[61]

Structural Description of HOFs 1a and 1b: Amine Effect on the Supramolecular Assemblies. We reported earlier the preparation and molecular structure of HOF **1a**, where **1** was cocrystallized in the presence of 2 equiv of DABCO to generate a higher order supramolecular structure.[61] However, in order to investigate in more detail the effect of the Lewis base on the resultant supramolecular arrangement, we cocrystallized **1** in the presence of 2 equiv of a less basic amine, namely, 4,4′-bpe to yield the HOF **1b**. It is noteworthy, that

DOI: 10.1021/acs.cgd.8b00030
Cryst. Growth Des. 2018, 18, 3805−3819

contrary to the observed in **1a**, the HOF **1b** always crystallizes as a solvate with a 1:1 diamine-alkoxysilanol stoichiometric ratio.

The X-ray crystallographic analysis of **1a** and **1b** reveals how the silanetriol moieties act as adhesive functional groups, where two of their three OH groups act as both donor and acceptor of the hydrogen bonds (SiO4−H4 and SiO2−H2 in **1a**; SiO4−H4A and SiO3−H3A in **1b**), whereas the third one acts only as a hydrogen bond donor (SiO3−H3 in **1a** and SiO2−H2A in **1b**). Consequently, in **1a** and **1b** the organo-bis(silanetriol) molecules are linked end-to-end through the formation of highly directional hydrogen-bonding interactions between the $Si(OH)_3$ moieties, where the final supramolecular synthon can be described according to the graph set theory by the $R_2^2(8)$ eight-membered ring motif (Figure 1a and Figure 2a).[17,18] This self-association leads to the formation of infinite 1D supramolecular chains, which propagate along the crystallographic *c*-axis in a $C_2^2(26)$ pattern in terms of the graph set analysis (Figure 1b and Figure 2b).[17,18] The corresponding D···A distances and the ∠DHA angles are listed in Table 2.

In HOFs **1a** and **1b**, the insertion of the first equivalent of amine permits the interconnection of two neighboring chains leading to the formation of a ladder-like macrocyclic system. These macrocycles can be described as $R_4^4(36)$ and $R_6^6(52)$ ring motifs, respectively.[17,18] The relative size of such macrocycles (**1a**: $d_{Si\cdots Si}$ = 10.5 × 9.8 Å and **1b**: $d_{Si\cdots Si}$ = 10.5 × 17.9 Å) is governed by the length of the organic amine, as in both cases the size of the organic spacer between the silicate moieties is identical (Figure 1c and Figure 2c).

The formation of planar eight-membered $R_2^2(8)$ ring synthons is commonly observed in other supramolecular arrangements formed by the self-association of either carboxylic or boronic acid derivatives. However, it should be pointed out that in **1a** and **1b**, the $R_2^2(8)$ synthon has a chair-shaped conformation and compares to those observed in the case of other tetrahedral tectons, such as sulfonic (SO_3H) and phosphonic (PO_3H_2) acids.[34−50] Nonetheless, in the case of the $Si(OH)_3$ moieties, the presence of three protonated OH groups attached to the same tetrahedral silicon atom enriches their capacity as molecular tectons in terms of hydrogen bonding interactions, mainly because the cooperative hydrogen-bonding $[H\cdots O(H)-Si-OH\cdots O(H)]_2$ between neighboring $Si(OH)_3$ moieties increases the acidic character of the external protons[62] (SiO4−H4 for **1a** and SiO3−H3A for **1b**), which in turn act as single hydrogen-bond donors toward Lewis base molecules.

Consequently, the acidified external protons permit the insertion of the first equivalent of DABCO and 4,4′-bpe molecules in **1a** and **1b**, respectively, through the formation of SiO−H···N interactions. Because DABCO (pK_a of 8.82)[63] is a better Lewis base than 4,4′-bpe (pK_a of 5.9)[64] such interactions are stronger in **1a** than in **1b**, where the D···A distances are 2.658(2) Å (O4···N1) and 2.716(2) Å (O3···N1), respectively. Additionally, this observation is also in accordance with their IR spectra, where the band associated with the νO−H stretching vibration of the Si−OH groups is almost negligible in **1a**, while in **1b** this band appears shifted to a lower frequency ($\tilde{\nu}$ 3087 cm^{-1}) compared to that of free organo-bis(silanetriol) ($\tilde{\nu}$ 3128 cm^{-1}).[61]

The third OH group attached to the silicon center in **1a** (SiO3−H3) binds to the second DABCO molecule, to afford the double-pillared macrocycle arrangement, through the formation of additional SiO−H···N interaction, with D···A distance of 2.742(2) Å (O3···N2), which is 0.08 Å longer than that observed in the hydrogen-bonding interaction with the external protons (Table 2).

By contrast, in the molecular structure of **1b**, the third OH group acts as a hydrogen-bond donor for a THF molecule. Therefore, **1b** keeps a single-pillared macrocycle arrangement, where in order to achieve a close-packed structure, a second molecule of THF fills the empty space within the macrocycle. Only weak C−H···O (3.593(1) Å, C···O) interactions can be observed between this THF molecule and the neighboring organic fragments (Figure 2c).

Subsequently, in **1a** and **1b**, complete 2D supramolecular networks are constructed by the multiplication of either the double- or the single-pillared macrocycles, respectively (Figure 1d and Figure 2d).

Finally, the 3D structure is generated by ABABAB stacking of these layers along the *a* and *b* crystallographic axes, respectively (Figure 3a,b). In both cases, the 3D arrangements are held together by weak intermolecular interactions between the adjacent 2D layers. Hence, in **1a**, there are C−H···π interactions between the DABCO molecules within one 2D layer and the aryl group of the organic *linker* in the adjacent layer, whereas in **1b**, C−H···O interactions between the hydrogen atoms of the pyridine rings in 4,4′-bpe and the oxygen atoms (O2 and O4) of the silanetriol moieties are observed.

It is noteworthy that the almost parallel stacking of the 2D layers, in **1b**, results in the formation of uniform 1D THF-filled channels running parallel to the crystallographic *b*-axis, whose window dimension is approximately 12.9 × 6.5 Å. The contact surface of the channels was calculated with a probe radius of 1.2 Å and grid spacing of 0.2 Å within Mercury to be 44% of the whole crystal volume (Figure 3c).

Structural Description of HOFs 2a and 2b: Effect of the Size of the Organic Spacer on the Supramolecular Assemblies. To investigate how the size of the organic spacer in the organo-bis(silanetriol) affects the porosity of the supramolecular arrangement, the precursor **2** was tested as a molecular tecton for the construction of multicomponent HOFs. Therefore, following the procedure used for the synthesis of HOFs **1a** and **1b**, compound **2** was cocrystallized with 2 equiv of DABCO and 4,4′-bpe to yield the HOFs **2a** and **2b**, respectively. The D···A distances and the ∠DHA angles are listed in Table 2.

In both structures, the self-association between adjacent silicate moieties through the formation of the robust $R_2^2(8)$ ring synthon was observed (Figure 4a and Figure 5a) leading to the formation of 1D supramolecular infinite chains described by the $C_2^2(34)$ graph set motif (Figure 4b and Figure 5b).[17,18] In analogy to **1a** and **1b**, in HOFs **2a** and **2b**, the formation of the SiO−H···N interactions between the more acidic external protons and the corresponding amine molecule results in the creation of supramolecular macrocycles that can be described by the $R_4^4(44)$ and $R_4^4(56)$ ring motifs, respectively (Figure 4c and Figure 5c).[17,18] However, due to the presence of longer organic bridging group in the organosilicate tecton **2**, these macrocycles are bigger (**2a**: $d_{Si\cdots Si}$ = 14.6 × 9.6 Å and **2b**: $d_{Si\cdots Si}$ = 14.5 × 17.1 Å) than those exhibited in the crystalline structures derived from the organosilicate tecton **1** (**1a**: $d_{Si\cdots Si}$ = 10.5 × 9.8 Å and **1b**: $d_{Si\cdots Si}$ = 10.5 × 17.9 Å).

The above-mentioned SiO−H···N interactions are stronger in **2a** (2.653(2) Å, O2···N1) than those observed in **2b** (2.705(2) Å, O2···N1). Interestingly, in compounds **2a** and **2b**,

DOI: 10.1021/acs.cgd.8b00030
Cryst. Growth Des. 2018, 18, 3805−3819

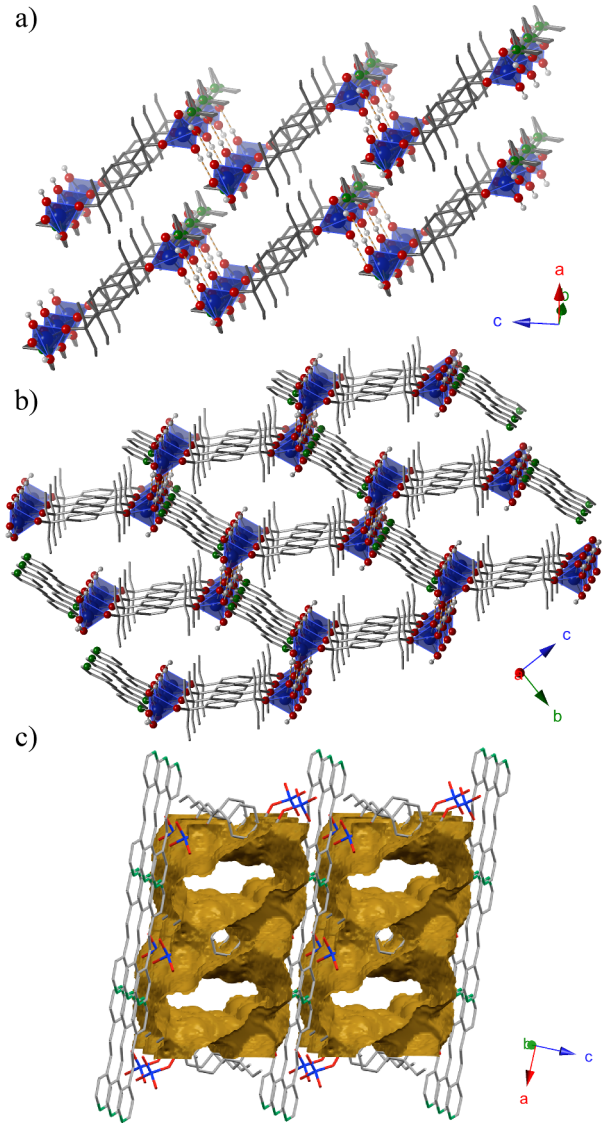

Figure 3. (a) 3D supramolecular arrangement of HOF **1a** formed by the ABAB stacking of the 2D layers along the crystallographic *a*-axis. (b) 3D supramolecular arrangement of HOF **1b**. (c) Porous structure of HOF **1b** with 1D channels running parallel to the crystallographic *b*-axis.

the third hydroxyl group interacts with a second diamine molecule through SiO−H···N interactions 2.699(2) Å (O3···N2) and 2.736(2) Å (O4···N2), respectively, leading to the formation of extended double-pillared supramolecular networks (Figure 4d and Figure 5d). Finally, in both HOFs, the double-pillared hydrogen-bonded layers are further packed in an ABABAB arrangement affording the corresponding 3D structures (Figure S1 and Figure S2).

The comparison between the supramolecular arrangements in **1a** and **2a** clearly reveals that the presence of a longer organic bridging group in the organosilicate tecton **2** did not affect the self-assembly process between the complementary tectons, but it modifies the resultant 3D supramolecular network. While **1a** does not contain solvent molecules within the network, **2a** exhibits the formation of 0D voids filled by THF molecules, interacting via C−H···π (2.900(1) Å, 129.1(1)°) contacts with the organic spacer (Figure 6a).

On the other hand, the comparison between the supramolecular arrangements of **1b** and **2b** reveals that the increase in the size of the organic bridging group affects the self-assembly process of the complementary diamine-silanol tectons. Thus, while **1b** shows the formation of single-pillared hydrogen-bonded layers, **2b** exhibits the insertion of the second equivalent of 4,4′-bpe, leading to the formation of double-pillared hydrogen-bonded layers. Additionally, the supramolecular arrangement of HOF **1b** contains 1D channels filled by THF molecules, whereas in the HOF **2b** the solvent molecules are enclosed in 0D voids formed between two neighboring supramolecular layers, where the THF molecules interact with the neighboring organic fragments via C−H···π (2.90(1) Å) and C−H···O (2.542(1) Å, 161(1)°) contacts (Figure 2c).

Structural Description of HOFs 3a and 3b: Effect of Available OH Groups. Finally, the role of the number of the OH groups in each silicate moiety during the self-assembly process toward the formation of diamine-silanol based HOFs was evaluated. For this purpose, the organo-bis(silanediol) **3** $(HO)_2(^tBuO)Si-O-R-O-Si(O^tBu)(OH)_2$ (R = 1,4-$[CEt_2]_2C_6H_4$) was tested as a molecular tecton, because this compound is an analogue to **1** in terms of the size and rigidity of the organic bridging group. However, one of the three OH groups of each $Si(OH)_3$ moiety has been blocked by replacing it by a ^{t}BuO group. Therefore, the cocrystallization of **3** in the presence of 2 equiv of DABCO or 4,4′-bpe afforded the HOFs **3a** and **3b**, respectively.

In the case of **3a**, the formation of a HOF with a 2:1 diamine-silanol stoichiometric ratio was observed. The most striking change was the absence of the $R_2^2(8)$ synthon, which was recurrently present in the previous HOFs. Instead, the diamine molecules are inserted between the silicate moieties through SiO−H···N interactions, where the D···A distances are 2.655(2) Å (O3···N1) and 2.672(2) Å (O4···N2) (Figure 7a). These interactions give rise to a supramolecular macrocycle that is comprised of intercalated amine−silicate molecules and can be described by the $R_4^4(36)$ ring motif with $d_{Si\cdots Si}$ spacing of 10.5 × 10.1 Å (Figure 7b).[17,18] The consecutive formation of such macrocycles leads to the formation of 1D supramolecular strands running along the crystallographic *b*-axis (Figure 7c). Such 1D strands are surrounded by solvent molecules, which form weak van der Waals interactions holding the whole crystal together in the other two directions.

The HOF **3b** crystallized with a 1:1 diamine-silanol stoichiometric ratio, and the supramolecular structure of the latter is completely different from that described for **3a**. First, although the eight-membered $R_2^2(8)$ synthon is not present, the OH groups of the silanediol moieties participate in SiO−H···O hydrogen-bonding interactions with other two neighboring molecules of **3** with a D···A distance of 2.846(1) Å (O4···O3), leading to the formation of a $C_1^1(4)$ supramolecular chain running along the crystallographic *b*-axis (Figure 8a).[17,18] These chains are interconnected by the organic bridging groups of the organosilyl tectons, thereby creating a $R_4^4(34)$ ring motif comprised of only organo-bis(silanediol) molecules.[17,18] Such a ring motif is extended parallel to the crystallographic *bc* plane leading to the formation of 2D supramolecular layers (Figure 8b). Next, the H3 proton of the silanediol moiety is involved in another hydrogen-bonding interaction with a 4,4′-bpe molecule (2.746(8) Å, O3···N1), to yield a close-packed 3D supramolecular network (Figure 8c).

DOI: 10.1021/acs.cgd.8b00030
Cryst. Growth Des. 2018, 18, 3805−3819

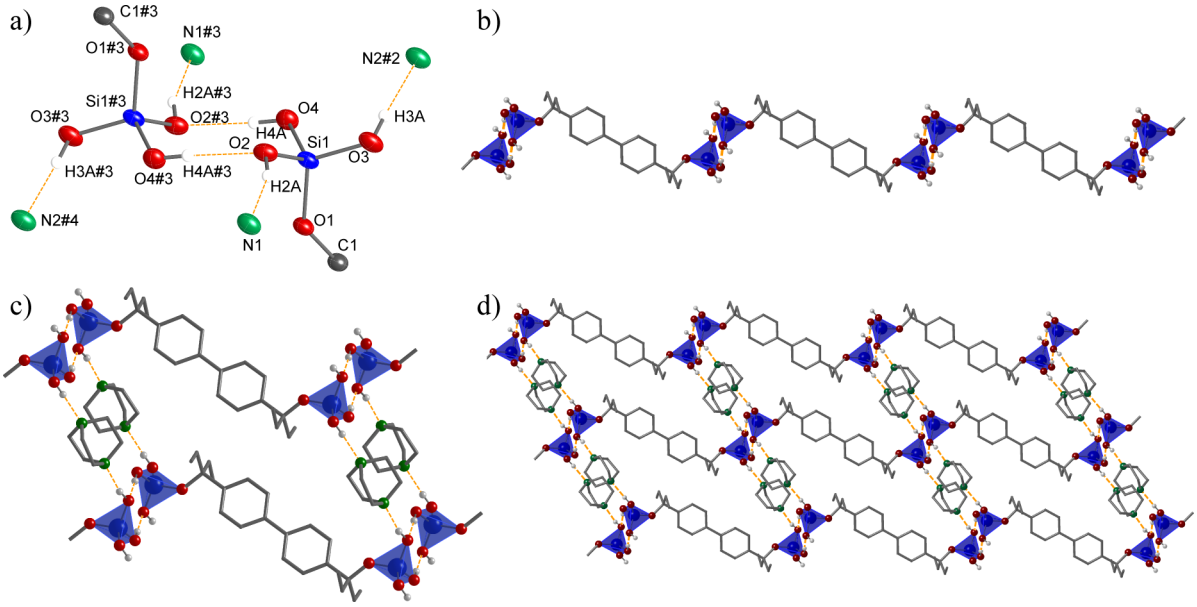

Figure 4. Supramolecular arrangement in HOF **2a**. (a) The $R_2^2(8)$ chair-shaped ring motif. Symmetry codes to generate equivalent positions: #2: x, 1 + y, z; #3: 1 − x, 1 − y, −z; #4: 1 − x, −y, −z. (b) The $C_2^2(34)$ motif. (c) The $R_4^4(44)$ diamine-silanol macrocycle. (d) 2D supramolecular network constructed from the diamine-silanol macrocycles.

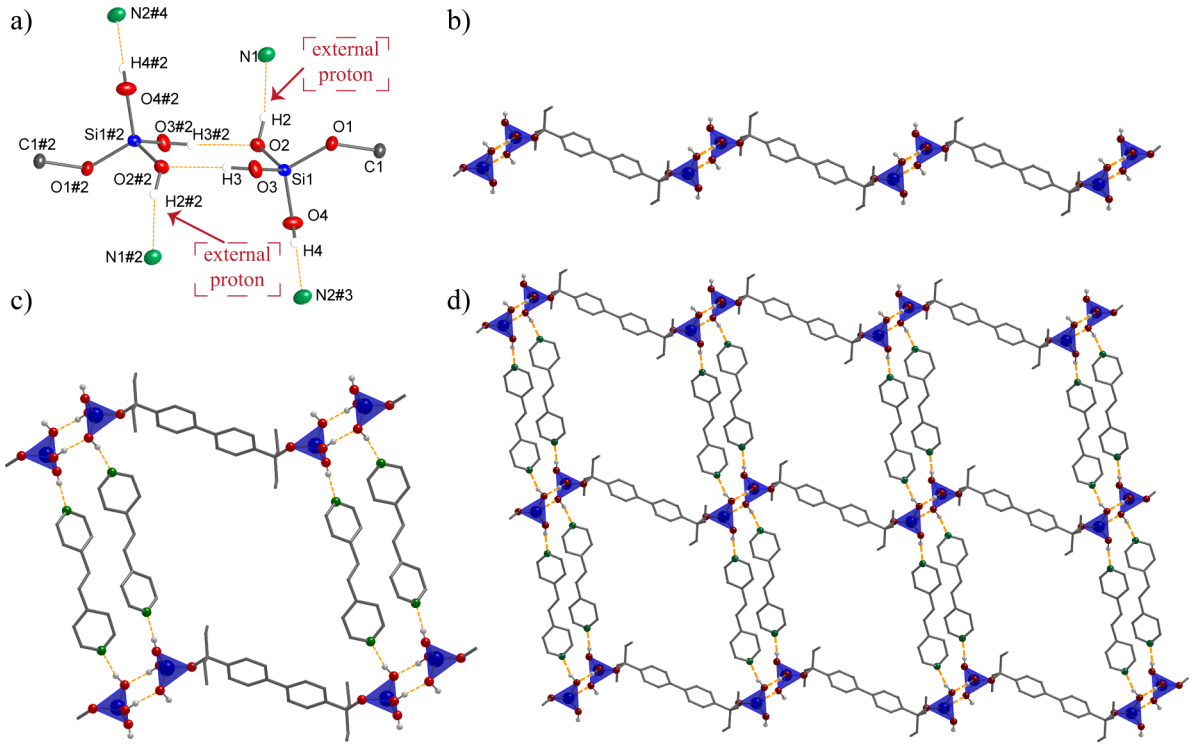

Figure 5. Supramolecular arrangement in HOF **2b**. (a) The $R_2^2(8)$ chair-shaped ring motif. Symmetry codes to generate equivalent positions: #2: 2 − x, −y, −z; #3: 1 + x, − 2 + y, z; #4: 1 − x, 2 − y, −z. (b) The $C_2^2(34)$ motif. (c) The $R_4^4(56)$ diamine-silanol macrocycle. (d) 2D supramolecular network constructed from the diamine-silanol macrocycles.

In **3a** and **3b**, the relative strength of the hydrogen bonds formed by the diamine−silanol interactions is in accordance with their IR spectra. In **3a**, the band of the νO−H stretching vibration of the silanol groups is shifted to a lower frequency and is superimposed with the bands associated with the CH_3 stretching vibrations ($\tilde{\nu}$ 2966−2878 cm^{-1}), whereas in the IR spectra of **3b** the band associated with the νO−H stretching vibration is clearly identifiable at upper wavenumber ($\tilde{\nu}$ 3436 cm^{-1}, see Experimental section).

Comparative View: −Si(OH)$_3$ versus −Si(O^{t}Bu)(OH)$_2$ Moieties. The foregoing description of the crystalline structures of **1a**, **1b**, **2a**, **2b**, **3a**, and **3b** provides an opportunity to examine how the Brønsted acidity of the silanol groups and the steric hindrance around the silicon center affect their hydrogen-bonding interactions either via self-association or

DOI: 10.1021/acs.cgd.8b00030
Cryst. Growth Des. 2018, 18, 3805−3819

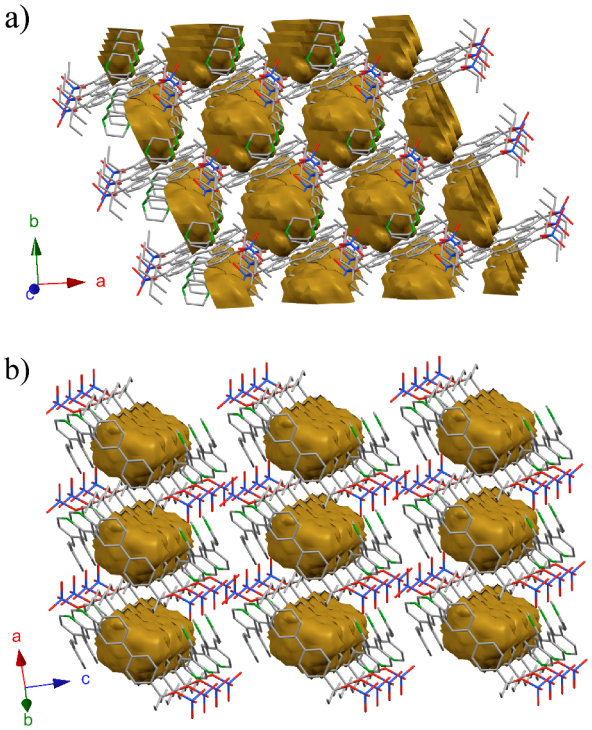

Figure 6. Formation of 0D voids within the supramolecular assemblies of HOFs **2a** (a) and **2b** (b).

with the amines. Consequently, it is evident that such binary supramolecular arrangements are vulnerable to subtle changes in the steric and electronic properties of their molecular building blocks, which allows modulating the porosity of the resulting hydrogen-bonging network (Table 3).

Thus, the major difference between the HOFs derived from organo-bis(silanetriols) **1** and **2** (**1a**, **1b**, **2a**, and **2b**) and those derived from the organo-bis(silanediol) **3** (**3a** and **3b**) is the degree of self-association between the silicate moieties because, while the first group exhibits the formation of the robust eight-membered $R_2^2(8)$ ring synthon, the second group shows weaker or no interactions between the silicate moieties.

This behavior might be rationalized taking into account the importance of the kinetic aspects during the crystallization process, as it is well-known that those interactions that are more probable to form first in the solution will dominate the first stage of the building up process.[16] Consequently, the formation of robust synthons, with strong and directional interactions, is a probabilistic event. Hence, once they are formed, they will not dissolve easily, and their existence is mediated by the variable interplay of the chemical and geometrical recognition aspects. Additionally, it is important to consider the critical role of the solvation and desolvation processes in the formation of solution-phase intermolecular interactions.[62]

Given all these considerations, in **1a**, **1b**, **2a**, and **2b**, the presence of the Si−OH···O hydrogen bonds forming the $R_2^2(8)$ synthon, rather than the more favorable strongest donor to strongest acceptor SiO−H···N interactions, may be explained by the tendency of silanol groups to the self-association even in solution. This fact has been demonstrated previously by Franz and co-workers.[62] By contrast, in the case of HOFs **3a** and **3b**, when one OH group of the silicate moiety is replaced by a bulky ^{t}BuO group, not only is the steric hindrance around the silicon center enhanced, but also the Brønsted acidity of the Si−OH groups suffers a decrement.[60] Therefore, it might be possible that the synergistic effect of the aforementioned two factors reduces the possibility of solution-phase aggregation between neighboring $Si(O^tBu)(OH)_2$ moieties. Consequently, in the case of these HOFs obtained from the tecton **3**, the interaction hierarchy (strongest donor to strongest acceptor) between Si−OH groups and amines gains more relevance during the firsts steps of the building up process. In the case of HOFs **1a**, **1b**, **2a**, and **2b**, the self-association between the $Si(OH)_3$ moieties into the $R_2^2(8)$ synthon is kinetically preferred and dominates the first stage of the assembly process.

Additionally, it is also important to take into account the role of the Lewis base during the construction of the diamine-silanol assemblies. Although the crystalline structure of the free organo-bis(silanediol) **3** exhibits the formation of the $R_2^2(8)$ homosynthon,[61] this self-association tendency can be gradually diminished by increasing the Lewis basicity of the amine tecton. Therefore, as was observed in the molecular structure of **3b**, the $R_2^2(8)$ ring synthon is partially opened by the insertion of 4,4′-bpe molecules. Hence, in this structure, each $Si(O^tBu)(OH)_2$ moiety binds to another two molecules of **3** where one of the OH groups acts only as a hydrogen-bond donor toward a neighboring silanediol moiety through the formation of a weak SiO−H···O interaction, whereas the second OH group acts as both the hydrogen-bond acceptor binding a second molecule of **3** and as a hydrogen-bond donor toward the 4,4′-bpe molecule.

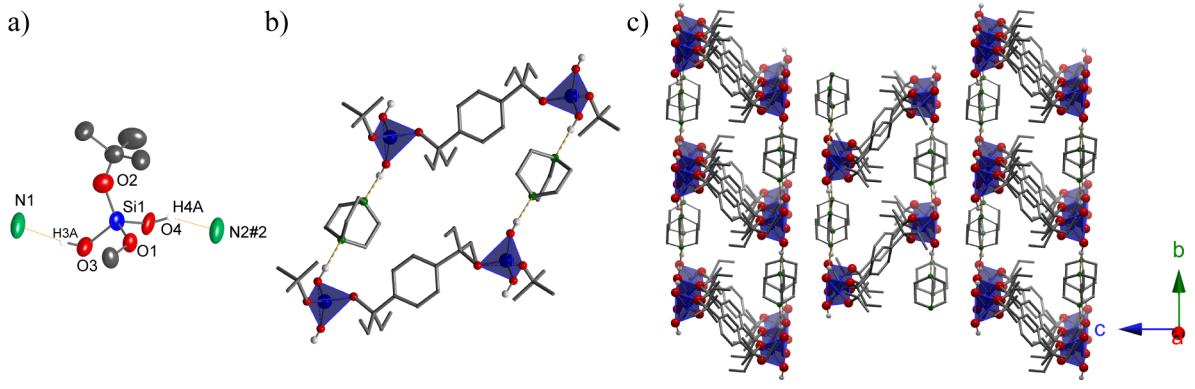

Figure 7. (a) SiO−H···N interactions found in the HOF **3a**. Symmetry codes to generate equivalent positions: #2: $x, -1 + y, z$. (b) The $R_4^4(36)$ ring motif. (c) 1D supramolecular strands running along the crystallographic *b*-axis. The solvent molecules have been omitted for clarity.

DOI: 10.1021/acs.cgd.8b00030
Cryst. Growth Des. 2018, 18, 3805−3819

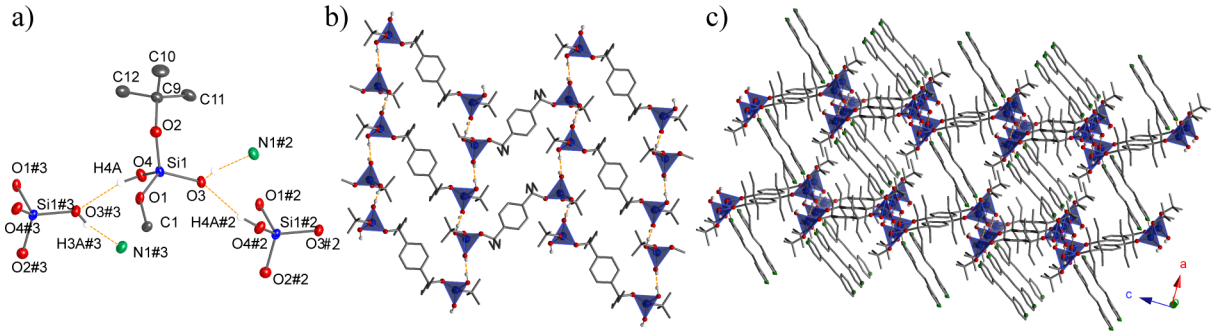

Figure 8. (a) Hydrogen-bonded interactions found in the HOF **3b**. Symmetry codes to generate equivalent positions: #2: $1 - x$, $-0.5 + y$, $0.5 - z$; #3:$1 - x$, $0.5 + y$, $0.5 - z$. (b) The 2D supramolecular layers formed by the $R_4^4(34)$ ring motifs extended parallel to the crystallographic *bc* plane. (c) Close-packed 3D hydrogen-bonded network.

Table 3. Comparison of Selected Parameters for HOFs 1a−3b

HOF	diamine-alkoxysilanol ratio	size of the macrocycle $d_{Si\cdots Si}$ (Å)	graph set motif[a]	THF molecules[b]	porosity	dimensionality of the HB arrangement
1a	2:1	10.5 × 9.8	$R_4^4(36)$	0	nonporous	2D
1b	1:1	10.5 × 17.9	$R_6^6(52)$	2	1D channels	2D
2a	2:1	14.6 × 9.6	$R_4^4(44)$	1	0D voids	2D
2b	2:1	14.5 × 17.1	$R_4^4(56)$	1	0D voids	2D
3a	2:1	10.5 × 10.1	$R_4^4(36)$	1	1D channels	1D
3b	1:1	5.4 × 10.5	$R_4^4(34)$	0	nonporous	3D

[a]Diamine-alkoxysilanol macrocycle. [b]Number of solvent molecules in the asymmetric unit.

This arrangement gives rise to the formation of a close-packed 3D structure.

By contrast, in the case of **3a**, the increase in the basicity of the amine tecton gives rise to the formation of only SiO−H···N interactions, and by consequence the absence of the $R_2^2(8)$ synthon. This results in the reduction of the overall dimensionality of the supramolecular arrangement from 3D in **3b** to 1D in **3a**, where the free space between such 1D diamine-silanol ribbons is filled by THF molecules.

Similarly, when the structural arrangements of HOFs **1a**, **1b**, **2a**, and **2b** are compared, the effect of the relative strength of the Lewis base and the size of the organic spacer on the porosity of the network can be observed. As mentioned earlier, the cooperative hydrogen-bonding association between two $Si(OH)_3$ moieties enhances the acidic character of the two external protons that do not participate in the dimeric $R_2^2(8)$ ring. Consequently, considering that at this point of the self-assembly process the SiO−H···N interactions are more relevant, the first equivalent of the amine is incorporated into the supramolecular arrangement. Nevertheless, the insertion of the second equivalent will be determined by the subtle interplay between the geometrical and chemical aspects. As it was observed in the structures of **1a**, **2a**, and **2b**, at this stage of the building up process, the chemical aspects are the principal driving force in the formation of the supramolecular arrangement leading to the insertion of the second equivalent of amine molecules to yield a double-pillared 2D layered arrangement. By contrast, in **1b**, after the insertion of the first equivalent of 4,4′-bpe molecules between the organosilicate 1D chains, the geometrical aspects gain more relevance, and a close-packed structure is obtained without the inclusion of the second equivalent of 4,4′-bpe leading to the formation of a single-pillared 2D arrangement. This structural modularity was achieved by reducing the basic character of the amine and shortening the distance between the silicate moieties in the organosilicate tecton. This is based on the reasoning that when one of these two variables is modified using a stronger base, as in **1a**, or larger organic bridging group as in **2b**, the expected 2:1 diamine-alkoxysilanol stoichiometric ratio is maintained.

Powder X-ray Diffraction. The powder X-ray diffraction (PXRD) analysis of the bulk samples of HOFs **1a**, **2a**, **2b**, and **3b** was used to confirm their phase purity, as the experimental PXRD diffractograms match well with those simulated from their single crystal X-ray diffraction data (Figures S3−S6). On the contrary, a minimal agreement was observed between the experimental and simulated PXRD patterns of HOFs **1b** and **3a** (Figures S9 and S10). It is known that in porous materials the loss of solvent molecules occupying the channels can lead to a partial or complete collapse of the structure.[65,66] This is more pronounced in HOFs because the tectons are held together only by weak hydrogen bonds. Therefore, the incongruences between the experimental (powder sample exposed for 4 h to high vacuum) and simulated PXRD patterns for **1b** and **3a** could be explained by the presence of 1D channels filled with THF molecules. It is noteworthy that in the case of **1b** even a short air drying causes a significant loss of crystallinity. To test this hypothesis, we first measured unit cells of a variety of single crystals from the recrystallized samples of **1b** and **3a** at 100 K to assess the phase purity of the bulk of the crystals without the risk of solvent loss. Next, a monocrystal of the respective HOF was glued on a glass fiber in a way that most of its surface remained free. A small subset of X-ray data was collected at 100 K to confirm again that the crystal belongs to the studied HOF. After that, the same measurement was performed at 298 K to exclude that a temperature induced phase change is responsible for the difference between the simulated and experimental powder diffractograms, but only an expansion of 3.8 and 5.7% (for **1b** and **3a**) of the unit cell was observed (Table S2). The degradation of the crystals was monitored by collecting further data at different times (10 min and 1 h on air) until finally four

DOI: 10.1021/acs.cgd.8b00030
Cryst. Growth Des. 2018, 18, 3805−3819

frames at different theta/2theta geometry were acquired, and the Debye rings were integrated within the APEX 3 program to obtain the corresponding diffractograms (Figures S7 and S8). Furthermore, the same measurement was made after 4 h under a vacuum for **3a** and because the crystal **1b** disintegrates when exposed to a vacuum the measurement for **1b** was repeated after 18 h on air. Figures S9 and S10 in the Supporting Information contain the comparison between the simulated and the different experimental powder diffractograms and show the stepwise change in the crystallinity and transformation of the phases. Importantly, the diffractograms obtained from the monocrystals do not fully agree with those from the bulk samples, but they can be marked as intermediates as they can be traced in those of the bulk samples. Finally, the elemental analysis of the bulk samples of **1b** and **3a** confirms the complete (**1b**) and partial (**3a**) THF loss, but most importantly the retention of the bis(silanol):amine stoichiometry even in the desolvated samples.

Gas-Sorption Experiments. Typically, porous hydrogen-bonded supramolecular networks collapse once the solvent guest molecules are removed after a thermal and/or vacuum activation. This is mainly because the hydrogen bonding interactions are commonly too weak to support the entire structure and stabilize the network. Consequently, in this work the extrinsic porosity and the strength of the hydrogen bonding interactions between the complementary tectons in HOF **1b** prompted us to examine its permanent porosity. For this purpose, N_2 sorption experiments were performed. Prior to any gas adsorption experiment, samples of HOF **1b** were activated at 353 K and 10^{-3} bar for 1 h. Then, the very low N_2 uptake (estimated BET are of 8 $m^2\ g^{-1}$) at the cryogenic temperature of 77 K suggested two possibilities: (i) there is no access to any permanent porosity within the HOF **1b** or (ii) HOF **1b**, selectively, did not adsorb N_2 even at 77 K. To elucidate these prospects, isothermal CO_2 adsorption experiments (increasing the partial pressure from 0 to 100 kPa at 196 K) were carried out. The adsorption of CO_2 at 303 K is indeed complicated since it is very close to the critical temperature of CO_2.[67] At 303 K the density (δ_{CO_2}) of adsorbed CO_2 is difficult to estimate because the CO_2 saturation pressure is really high and therefore, the range of P/P_0 is limited to only 0.02 at subatmospheric pressures.[68] Thus, when the CO_2 isotherm was completed, CO_2 was found to be adsorbed in activated HOF **1b** at 196 K (0.44 mmol·g^{-1}), see (Figure 9a), suggesting CO_2 selectivity. After the CO_2 sorption experiment was finished, the retention of the crystallinity on HOF **1b** was corroborated by PXRD (see Figure S11). CO_2 selectivity over N_2 (at cryogenic temperatures) has been before observed in similar crystalline structures such as PCM-14,[69] CUK-1,[70] the metal-macrocycle framework NMC-1,[71] and a carbazole-based supramolecular polyhedron structure.[72]

A strong hysteresis loop was observed with marked stepped profiles in the desorption profile (Figure 9a, open circles). The window dimensions of HOF **1b** (~12.9 × 6.5 Å) are significantly larger than the kinetic diameter of CO_2 (3.3 Å). Thus, this hysteresis cannot be associated with a "kinetic trap" argument as previously suggested for similar materials.[73−75] Instead, the observed hysteresis might be due to the relatively strong host−guest interactions (at 196 K) and the flexible nature of HOF **1b**. The last desorption point in the isotherm (Figure 9a) indicates an incomplete CO_2 desorption process at 196 K. In other words, this suggests that some CO_2 molecules

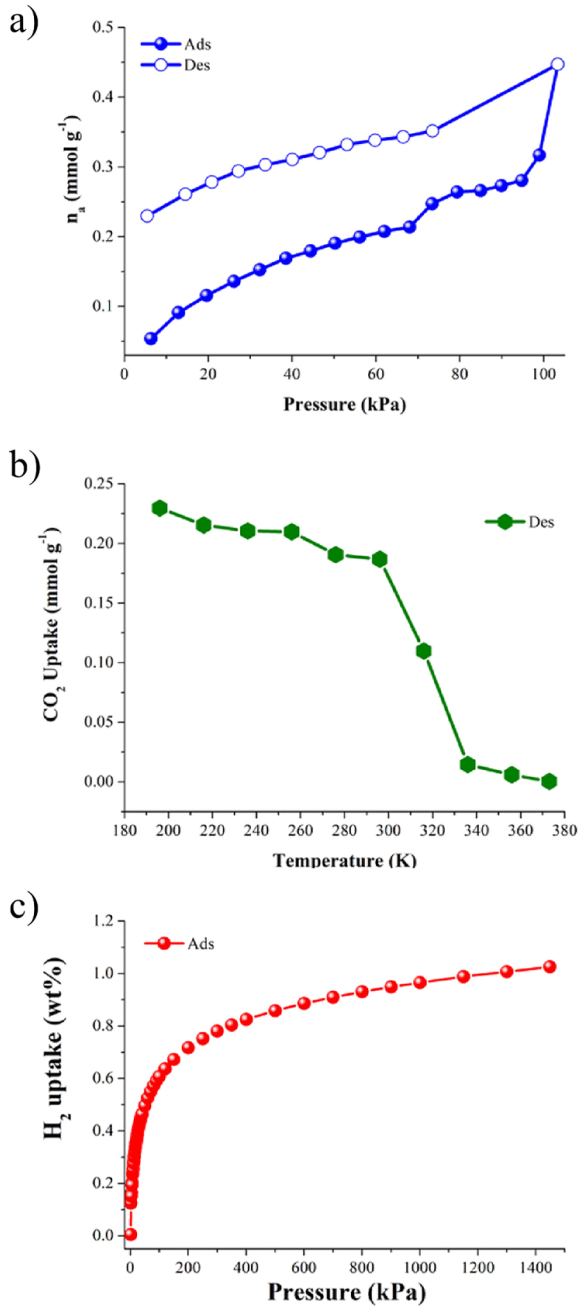

Figure 9. (a) CO_2 adsorption−desorption isotherm of HOF **1b** at 196 K (adsorption closed circles, desorption open circles, (b) CO_2 desorption while increasing the temperature, (c) H_2 adsorption isotherm for HOF **1b** at 77 K.

remained trapped inside the pores of HOF **1b**. To corroborate our hypothesis, we performed another experiment where after the adsorption−desorption CO_2 isotherm was completed (at 196 K), we gradually increased the temperature up to 373 K and monitored the desorption process (Figure 9b). Then, from 196 to 296 K the CO_2 uptake was only reduced from 0.23 mmol g^{-1} to 0.19 mmol g^{-1}, verifying that the CO_2 molecules were confined inside the cavities of HOF **1b** and not on the surface.[76] From 296 to 336 K, a considerable drop in the CO_2 uptake was observed (from 0.19 mmol g^{-1} to 0.01 mmol g^{-1}) to last desorb the CO_2 completely at 373 K (Figure 9b).

Nevertheless, the retention of CO_2 within the hydrogen-bonded network is not associated with the formation of

DOI: 10.1021/acs.cgd.8b00030
Cryst. Growth Des. 2018, 18, 3805−3819

carbamates. It is well-known that, unlike primary and secondary amines, tertiary amines do not form stable carbamates, as the lack of the free proton on the nitrogen atom of these amines inhibits the carbamate formation, and under wet conditions, an alternate reaction leads to the formation of bicarbonate ions.[77] Moreover, the absence of carbamates in the system is fully supported by the infrared spectroscopy measurements performed on HOF **1b**: as-synthesized, after activated at 80 °C, and after CO_2 exposure (Figure S12). These FT-IR spectra are essentially equal and neither from the typical vibration bands of the carbamate moiety, including the asymmetric (ν_{asCOO}^-, $\tilde{\nu}$ 1600−1500 cm^{-1}) and symmetric (ν_{sCOO}^-, $\tilde{\nu}$ 1450−1350 cm^{-1}) vibrations of the COO^- moiety, as well as the N−COO^- stretching vibration (ν_{N-COO}^-, $\tilde{\nu}$ 1300−1260 cm^{-1}), were observed after the exposure of the framework to CO_2.[78,79]

Finally, an activated sample of HOF **1b** (vide supra) was tested for H_2 adsorption at 77 K (Figure 9c), where the H_2 adsorption for HOF **1b** exhibits a typical isotherm Type I and a total H_2 uptake of 1.0 wt % at 1450 kPa and 77 K. Interestingly, this uptake is competitive with similar crystalline materials.[80]

Thermal Stability. The thermal stability of the obtained HOFs was studied by TGA under nitrogen atmosphere (Figure 10). The thermal decomposition of **1a** occurs in two stages,

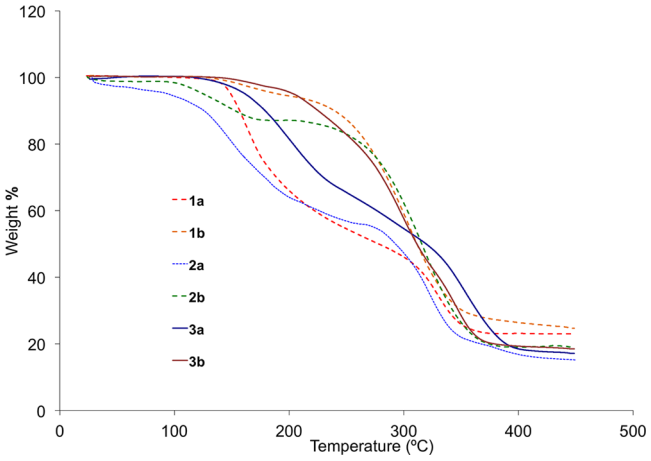

Figure 10. TGA trace of HOFs **1a**, **1b**, **2a**, **2b**, **3a**, and **3b**.

where the first stage (temperature range 130−275 °C) may be associated with the condensation of $Si(OH)_3$ moieties accompanied by the thermal decomposition of the DABCO molecules. This assumption was made taking into account the reported thermal decomposition of free DABCO within this temperature range (75−250 °C).[81] The second stage corresponds to a decomposition of the organic bridging group, which leads to the formation of hydrated silica $2SiO_2 \cdot H_2O$[82] as residual mass at 450 °C (observed residual weight: 22.8%, calculated residual weight: 21.9%). By contrast, in **1b** the interchange of DABCO by 4,4′-bpe increases the thermal stability of the resultant supramolecular arrangement. Thus, although the thermal condensation of the $Si(OH)_3$ moieties takes place in a temperature range of 125−175 °C (observed weight loss: 5.9%, calculated weight loss: 6.1%), the thermal decomposition of the organic backbone takes place in a temperature range of 200−450 °C (observed weight loss: 69.7%, calculated weight loss: 73.1%). This leads to the formation of silica $2SiO_2$ as residual mass at 450 °C (observed residual weight: 24.4%, calculated residual weight: 20.4%). It is noteworthy that the thermogravimetric curve of **1b** does not show the solvent release, even though there are THF molecules filling the 1D channels within the supramolecular arrangement. This fact is also in accordance with the elemental analysis of **1b** obtained after being dried under a vacuum for 4 h, where the THF molecules were absent.

Conversely, the thermogravimetric curves of **2a** and **2b**, which also crystallized as solvates, confirm the release of the solvent molecules in the first stage of their thermograms. Therefore, the first stage of decomposition for **2a** (temperature range 75−250 °C) is attributed not only to the condensation of the $Si(OH)_3$ moieties and the thermal decomposition of DABCO molecules but also to the release of one molecule of THF (observed weight loss: 40.3%, calculated weight loss: 43.9%). Subsequently, the next step, observed between 250 and 375 °C, corresponds to the decomposition of the organic bridging groups (observed weight loss: 41.6%, calculated weight loss: 41.0%). This leads to the formation of hydrated silica $2SiO_2 \cdot H_2O$[82] as residual mass at 450 °C (observed residual weight: 15.2%, calculated residual weight: 17.0%).

Similarly, for **2b** the first step is observed between 75 and 200 °C and corresponds to the condensation of $Si(OH)_3$ moieties and the release of solvent molecules (observed weight loss: 13.1%, calculated weight loss: 11.8%). Consequently, the second stage (temperature range 200−450 °C) is associated with the thermal decomposition of the organic backbone (observed weight loss: 68.1%, calculated weight loss: 74.9%). This leads to the formation of silica $2SiO_2$ as residual mass at 450 °C (observed residual weight: 18.8%, calculated residual weight: 17.0%).

Finally, the thermograms of **3a** and **3b** show that their thermal decomposition is more complex and takes place through several stages giving rise to silica as residual mass at 450 °C. Additionally, in both cases the thermal decomposition of the organic backbone starts at a lower temperature (100 and 125 °C, respectively) than in their analogues **1a** and **1b**. This observation may be explained by the thermal lability of the ^{t}BuO groups, which can suffer a β-elimination process to afford isobutene. This fact is also in accordance with the relative thermal stability of the free organo-bis(silanols) **1** and **3** (Figure S13).

CONCLUSIONS

In summary, in this work, we presented new multicomponent hydrogen-bonded organic frameworks with adjustable supramolecular patterns and modular assembly. Such materials were obtained under mild reaction conditions using a binary design strategy through cocrystallization of organo-bis(silanols) with selected organic diamines, where such compounds act as complementary tectons. The structural analysis of these materials provides a systematic study about how subtle modifications in the molecular building blocks, such as size of the organic bridging group, the steric hindrance around the silicon center, the Brønsted acidity of the silanol groups, as well as the size and the basicity of the amine, may affect the variable interplay between the chemical and geometrical recognition aspects during the building up process. All materials based on organo-bis(silanetriol) tectons **1** and **2** (**1a**, **1b**, **2a**, and **2b**) exhibit the formation of the robust eight-membered $R_2^2(8)$ ring synthon through the self-association between the silicate moieties, mainly due to the presence and higher acidity of the third Si−OH group. On the contrary, replacing this third Si−OH group by a bulky Si−O^{t}Bu moiety and therefore

DOI: 10.1021/acs.cgd.8b00030
Cryst. Growth Des. 2018, 18, 3805−3819

reducing the acidity of the OH groups in the tecton **3** used for the formation of HOFs **3a** and **3b** lowers the degree of self-association between the silicate moieties, and the $R_2^2(8)$ ring synthon was not present. Furthermore, the structural comparison between **1a** (nonporous network) and **2a** (0D cavities within the lattice) shows that the size of the organic bridging group in the organosilicate tecton does not affect the self-assembly process between the complementary tectons, but it modifies the resultant 3D lattice. Additionally, the differences in the porosity of **1a**, **1b**, and **2b** can also be attributed to the synergistic effect of the size and basicity of the amine with the size of the organic spacer in the organosilanols-based tectons. This enables rational design of supramolecular assemblies, which in turn determines the formation of diamine-silanol hydrogen-bonding networks with tunable dimensionality.

Consequently, we demonstrated that this approach also allows the fine-tuning of the porosity of the network, as structures with nonporous arrangements (**1a** and **3b**), 0D voids (**2a** and **2b**), or one with 1D channels filled by THF molecules (**1b**) were formed. Moreover, the latter presents permanent porosity and retains a certain degree of crystallinity once the solvent guest molecules are removed. Although the structure of the networks changes, it shows a breathing behavior derived from its flexibility and exhibits selective adsorption of CO_2 over N_2.

Finally, this study not only demonstrates the feasibility of the binary design strategy to control both the structure and functionality of the resulting material, but these results also confirm the versatility of the organo-bis(silanols) as molecular building blocks, because unlike observed for other tectons with tetrahedral nodes, the organosilanol-based derivatives can have up to three OH groups attached to the same central atom. Moreover, in such derivatives, the functionality of the organic bridging groups and the steric and electronic properties of the silicate moieties can be readily adjustable.

Given all these considerations, it is evident that the organo-bis(silanols) represent a set of very promising molecular building blocks for the construction of multicomponent HOFs, as they open the possibility to introduce a wide variety of organic functionalities. Such studies are currently underway in our research group.

EXPERIMENTAL SECTION

General Remarks. The solvents were purchased from Sigma-Aldrich and dried prior use with an MBraun SPS solvent purification system using Grubs' columns. Organic diamines 1,4-diazabicyclo[2.2.2]octane (DABCO) and *trans*-1,2-bis(4-pyridyl)-ethylene (4,4′-bpe) were purchased from Sigma-Aldrich and used without further purification. The alkoxysilanols 1,4-$[(HO)_3SiOCEt_2]_2$-C_6H_4 (**1**) and 1,4-$[\{(HO)_2(^tBuO)Si\}OCEt_2]_2C_6H_4$ (**3**) were obtained by the hydrolysis of their corresponding acetoxysilylalkoxides as reported recently,[61] while 4,4′-$[(HO)_3SiOCEt_2]_2$-(1,1′-biphenyl) (**2**) was synthesized using an analogous procedure (see Supporting Information for details). Elemental analyses (C, H, N) were determined on an Elementar MicroVario Cube analyzer. FT-IR spectra were recorded on a Bruker ALPHA FTIR spectrometer using the ATR technique with a diamond window in the range of $\tilde{\nu}$ 500–4000 cm^{-1}. Melting points were measured on Büchi B-540 melting point apparatus. TGA measurements were carried on a Netzsch STA 449 F3 Jupiter with a heating rate of 10 °C/min from room temperature to 450 °C. The measurements were performed with a constant flow of dinitrogen gas (50 mL/min), using 5 mm aluminum crucible. A Savitzky-Golay smoothing algorithm was employed for the GA curves. N_2, CO_2, and H_2 isotherms were recorded on a Belsorp mini II and a Belsorp HP (high pressure) analyzers, respectively, under high vacuum in a clean system with a diaphragm and turbo pumping system. Powder X-ray diffraction patterns were measured on a Bruker D8 Advance X-ray diffractometer equipped with a LynxEye detector using CuK_α radiation (λ = 1.5406 Å; monochromator: germanium).

Synthesis of HOFs. ***1a***. A solution of DABCO (**a**) (0.11 g, 0.98 mmol) in THF (2 mL) was added to a solution of 1,4-$[(HO)_3SiOCEt_2]_2C_6H_4$ (**1**) (0.20 g, 0.49 mmol) in THF (10 mL), and the mixture was stirred for 15 min. The white precipitate was filtered off, and crystals of **1a** were grown from a saturated THF solution at −24 °C. Yield: 0.24 g, 0.37 mmol, 76%. M.p. > 350 °C (dec.). Elemental analysis (%) Calcd for $C_{28}H_{54}O_8Si_2N_4$ (630.93 g·mol^{-1}): C 53.34, N 8.88, H 8.56; Found: C 52.65, N 8.52, H 8.47. FT-IR (cm^{-1}) $\tilde{\nu}$ 2958, 2881 (w, C−H, CH_3, CH_2), 927 (s, Si−O).

1b. A solution of 4,4′-bpe (**b**) (0.45 g, 2.46 mmol) in THF (3 mL) was added to a solution of 1,4-$[(HO)_3SiOCEt_2]_2C_6H_4$ (**1**) (0.50 g, 1.23 mmol) in THF (15 mL), and the mixture was stirred for 15 min and saturated under a vacuum. Afterward, this mixture was stored at −24 °C to afford the HOF **1b** as a white crystalline solid, which was isolated by filtration. Yield: 0.63 g, 1.10 mmol, 87%. M.p. 290 °C (dec.). Elemental analysis (%) Calcd for $C_{28}H_{40}O_8Si_2N_2$ (588.80 g·mol^{-1}): C 57.12, H 6.85, N 4.76; Found: C 55.84, H 6.53, N 4.43. FT-IR (cm^{-1}) $\tilde{\nu}$ 3087 (s, SiO−H), 2960, 2880 (w, C−H, CH_3, CH_2), 925 (s, Si−O).

2a. A solution of DABCO (**a**) (0.23 g, 2.10 mmol) in THF (5 mL) was added to a solution of 4,4′-$[(HO)_3SiOCEt_2]_2$-(1,1′-biphenyl) (**2**) (0.50 g, 1.03 mmol) in THF (15 mL), and the mixture was stirred for 15 min. The white precipitate was filtered off, and crystals of **2a** were grown from a saturated THF solution at −24 °C. Yield: 0.55 g, 0.71 mmol, 69%. M.p. 250 °C (dec.). Elemental analysis (%) Calcd for $C_{34}H_{58}O_8Si_2N_4$·THF (779.14 g·mol^{-1}): C 58.58, H 8.54, N 7.19; Found: C 57.55, H 8.03, N 6.46. FT-IR (cm^{-1}) $\tilde{\nu}$ 3291 (s, SiO−H), 2934, 2876 (w, C−H, CH_3, CH_2), 916 (s, Si−O).

2b. A solution of 4,4′-bpe (**b**) (0.38 g, 2.10 mmol) in THF (5 mL) was added to a solution of 4,4′-$[(HO)_3SiOCEt_2]_2$-(1,1′-biphenyl) (**2**) (0.50 g, 1.03 mmol) in THF (15 mL), and the mixture was stirred for 15 min and saturated under a vacuum. Afterward, this mixture was stored at −24 °C to afford the HOF **2b** as a white crystalline solid, which was isolated by filtration. Yield: 0.74 g, 0.80 mmol, 78%. M.p. 270 °C (dec.). Elemental analysis (%) Calcd for $C_{46}H_{54}O_8Si_2N_4$·THF (919.14 g·mol^{-1}): C 65.33, H 6.80, N 6.10; Found: C 64.85, H 7.02, N 5.84. FT-IR (cm^{-1}) $\tilde{\nu}$ 3294 (s, SiO−H), 2932, 2876 (w, C−H, CH_3, CH_2), 919 (s, Si−O).

3a. A solution of DABCO (**a**) (0.13 g, 1.16 mmol) in THF (2 mL) was added to a solution of 1,4-$[\{(HO)_2(^tBuO)Si\}OCEt_2]_2C_6H_4$ (**3**) (0.30 g, 0.60 mmol) in THF (5 mL), and the mixture was stirred for 15 min and saturated under a vacuum. Afterward, this mixture was stored at −24 °C to afford the HOF **3a** as a white crystalline solid, which was isolated by filtration. Yield: 0.47 g, 0.53 mmol, 88%. M.p. 170 °C. Elemental analysis (%) Calcd for $C_{36}H_{70}N_4O_8Si_2$·0.35 THF (768.17 g·mol^{-1}): C 58.48, H 9.53, N 7.29; Found: C 57.75, H 9.68, N 7.23. FT-IR (cm^{-1}) $\tilde{\nu}$ 2966, 2938, 2878 (w, C−H, CH_3, CH_2), 919 (s, Si−O).

3b. A solution of 4,4′-bpe (**b**) (0.35 g, 1.92 mmol) in THF (5 mL) was added to a solution of 1,4-$[\{(HO)_2(^tBuO)Si\}OCEt_2]_2C_6H_4$ (**3**) (0.50 g, 0.96 mmol) in THF (7 mL), and the mixture was stirred for 15 min and saturated under a vacuum. Afterward, this mixture was stored at −24 °C to afford the HOF **3b** as a white crystalline solid, which was isolated by filtration. Yield: 0.51 g, 0.73 mmol, 76%. M.p. 165–168 °C. Elemental analysis (%) Calcd for $C_{36}H_{56}N_2O_8Si_2$ (701.02 g·mol^{-1}): C 61.68, H 8.05, N 4.00; Found: C 61.38, H 8.31, N 3.86. FT-IR (cm^{-1}) $\tilde{\nu}$ 3436 (s, SiO−H), 2969, 2936, 2877 (w, C−H, CH_3, CH_2), 924 (s, Si−O).

Single-Crystal X-ray Diffraction Analysis. Single crystals of all compounds were mounted on nylon loops and placed in the cold nitrogen stream (100 K) inside a Bruker APEX DUO diffractometer equipped with an Apex II CCD detector. Frames were collected using omega scans and integrated with SAINT.[83] Multiscan absorption correction (SADABS) was applied.[83] The structures were solved by using direct methods (SHELXT)[84] and refined using full-matrix least-squares on F^2 with SHELXL[85] using the ShelXle GUI.[86] Weighted *R*

DOI: 10.1021/acs.cgd.8b00030
Cryst. Growth Des. 2018, 18, 3805–3819

factors, R_w and all goodness-of-fit indicators are based on F^2. All non-hydrogen atoms were refined anisotropically. The hydrogen atoms of the C−H bonds were placed in idealized positions, whereas the hydrogen atoms from the OH moieties were localized from the difference electron density map, and their position was refined with U_{iso} tied to the parent atom with distance restraints (DFIX or SADI). The disordered groups and solvent molecules (**1b** 2 × THF; **2a** 1 × THF; **2b** 1 × THF, 1 × OH; **3a** 1 × ^{t}BuO, 1 × THF, 3 × Et; **3b** 1 × 4,4′-bpe, 2 × Et) were refined using geometry (SADI, SAME) and U_{ij} restraints (SIMU, RIGU) implemented in SHELXL.[85]

The molecular graphics were prepared using CrystalMaker,[87] Mercury,[88] and GIMP.[89]

■ ASSOCIATED CONTENT

Supporting Information

The Supporting Information is available free of charge on the ACS Publications website at DOI: 10.1021/acs.cgd.8b00030.

General experimental details for the synthesis of organo-bis(silanetriol) 4,4′-$[(HO)_3SiOCEt_2]_2$-(1,1′-biphenyl) (**2**), thermogravimetric analyses of compounds **1**, **2**, and **3**, PXRD patterns of HOFs **1a**, **1b**, **2a**, **2b**, **3a**, and **3b**, including HOF **1b** before and after CO_2 sorption experiments; as well as tables with selected Si−O bond lengths and O−Si−O angles (PDF)

Accession Codes

CCDC 1453231 and 1815223−1815227 contain the supplementary crystallographic data for this paper. These data can be obtained free of charge via www.ccdc.cam.ac.uk/data_request/cif, or by emailing data_request@ccdc.cam.ac.uk, or by contacting The Cambridge Crystallographic Data Centre, 12 Union Road, Cambridge CB2 1EZ, UK; fax: +44 1223 336033.

■ AUTHOR INFORMATION

Corresponding Author

*E-mail: vjancik@unam.mx. Fax: +52 (55) 56-16-22-17.

ORCID

Elí Sánchez-González: 0000-0002-5440-329X

Ilich A. Ibarra: 0000-0002-8573-8033

Vojtech Jancik: 0000-0002-1007-1764

Notes

The authors declare no competing financial interest.

■ ACKNOWLEDGMENTS

This work was supported by Dirección General de Asuntos del Personal Académico from UNAM (PAPIIT Grant IN205115) and CONACyT (Grant No. 179348). A. Núñez Pineda, L. Triana Cruz, N. Zavala Segovia, and U. Hernández Balderas are acknowledged for technical assistance. E.S.-G. thanks CONACyT (Grant No. 289042). I.A.I. thanks CONACyT (Grant No. 1789) and UNAM PAPIIT (Grant IN101517) for financial support. M.J.V.-H. is grateful to CONACyT for a Ph.D. scholarship (Grant No. 262860), while A.T.-H. acknowledges DGAPA-UNAM for postdoctoral fellowship.

■ REFERENCES

(1) Hu, F.; Liu, C.; Wu, M.; Pang, J.; Jiang, F.; Yuan, D.; Hong, M. *Angew. Chem., Int. Ed.* **2017**, *56*, 2101−2104.

(2) Li, P.; He, Y.; Arman, H. D.; Krishna, R.; Wang, H.; Weng, L.; Chen, B. *Chem. Commun.* **2014**, *50*, 13081−13084.

(3) Li, P.; He, Y.; Zhao, Y.; Weng, L.; Wang, H.; Krishna, R.; Wu, H.; Zhou, W.; O'Keeffe, M.; Han, Y.; Chen, B. *Angew. Chem.* **2015**, *127*, 584−587.

(4) Lü, J.; Perez-Krap, C.; Suyetin, M.; Alsmail, N. H.; Yan, Y.; Yang, S.; Lewis, W.; Bichoutskaia, E.; Tang, C. C.; Blake, A. J.; Cao, R.; Schröder, M. *J. Am. Chem. Soc.* **2014**, *136*, 12828−12831.

(5) Nugent, P. S.; Rhodus, V. L.; Pham, T.; Forrest, K.; Wojtas, L.; Space, B.; Zaworotko, M. J. *J. Am. Chem. Soc.* **2013**, *135*, 10950−10953.

(6) He, Y.; Xiang, S.; Chen, B. *J. Am. Chem. Soc.* **2011**, *133*, 14570−14573.

(7) Wang, H.; Bao, Z.; Wu, H.; Lin, R.-B.; Zhou, W.; Hu, T.-L.; Li, B.; Zhao, J. C.-G.; Chen, B. *Chem. Commun.* **2017**, *53*, 11150−11153.

(8) Dalapati, S.; Saha, R.; Jana, S.; Patra, A. K.; Bhaumik, A.; Kumar, S.; Guchhait, N. *Angew. Chem., Int. Ed.* **2012**, *51*, 12534−12537.

(9) Yang, W.; Yang, F.; Hu, T.-L.; King, S. C.; Wang, H.; Wu, H.; Zhou, W.; Li, J.-R.; Arman, H. D.; Chen, B. *Cryst. Growth Des.* **2016**, *16*, 5831−5835.

(10) Karmakar, A.; Illathvalappil, R.; Anothumakkool, B.; Sen, A.; Samanta, P.; Desai, A. V.; Kurungot, S.; Ghosh, S. K. *Angew. Chem., Int. Ed.* **2016**, *55*, 10667−10671.

(11) Lü, J.; Cao, R. *Angew. Chem., Int. Ed.* **2016**, *55*, 9474−9480.

(12) Adsmond, D. A.; Sinha, A. S.; Khandavilli, U. B. R.; Maguire, A. R.; Lawrence, S. E. *Cryst. Growth Des.* **2016**, *16*, 59−69.

(13) Goswami, P. K.; Thaimattam, R.; Ramanan, A. *Cryst. Growth Des.* **2016**, *16*, 1268−1281.

(14) Tothadi, S.; Sanphui, P.; Desiraju, G. R. *Cryst. Growth Des.* **2014**, *14*, 5293−5302.

(15) Desiraju, G. R. *Angew. Chem., Int. Ed. Engl.* **1995**, *34*, 2311−2327.

(16) Desiraju, G. R. *J. Am. Chem. Soc.* **2013**, *135*, 9952−9967.

(17) Etter, M. C.; MacDonald, J. C.; Bernstein, J. *Acta Crystallogr., Sect. B: Struct. Sci.* **1990**, *46*, 256−262.

(18) Bernstein, J.; Davis, R. E.; Shimoni, L.; Chang, N. *Angew. Chem., Int. Ed. Engl.* **1995**, *34*, 1555−1573.

(19) Hisaki, I.; Nakagawa, S.; Ikenaka, N.; Imamura, Y.; Katouda, M.; Tashiro, M.; Tsuchida, H.; Ogoshi, T.; Sato, H.; Tohnai, N.; Miyata, M. *J. Am. Chem. Soc.* **2016**, *138*, 6617−6628.

(20) Sarma, B.; Sanphui, P.; Nangia, A. *Cryst. Growth Des.* **2010**, *10*, 2388−2399.

(21) Durka, K.; Jarzembska, K. N.; Kamiński, R.; Luliński, S.; Serwatowski, J.; Woźniak, K. *Cryst. Growth Des.* **2012**, *12*, 3720−3734.

(22) Zhang, G.; Rominger, F.; Mastalerz, M. *Cryst. Growth Des.* **2016**, *16*, 5542−5548.

(23) Kutyła, S. E.; Stępień, D. K.; Jarzembska, K. N.; Kamiński, R.; Dobrzycki, Ł.; Ciesielski, A.; Boese, R.; Młochowski, J.; Cyrański, M. K. *Cryst. Growth Des.* **2016**, *16*, 7037−7050.

(24) Campos-Gaxiola, J. J.; García-Grajeda, B. A.; Hernández-Ahuactzi, I. F.; Guerrero-Álvarez, J. A.; Höpfl, H.; Cruz-Enríquez, A. *CrystEngComm* **2017**, *19*, 3760−3775.

(25) Moorthy, J. N.; Mandal, S.; Venugopalan, P. *Cryst. Growth Des.* **2012**, *12*, 2942−2947.

(26) Yang, W.; Wang, J.; Wang, H.; Bao, Z.; Zhao, J. C.-G.; Chen, B. *Cryst. Growth Des.* **2017**, *17*, 6132−6137.

(27) Zentner, C. A.; Lai, H. W. H.; Greenfield, J. T.; Wiscons, R. A.; Zeller, M.; Campana, C. F.; Talu, O.; FitzGerald, S. A.; Rowsell, J. L. C. *Chem. Commun.* **2015**, *51*, 11642−11645.

(28) Hisaki, I.; Ikenaka, N.; Gomez, E.; Cohen, B.; Tohnai, N.; Douhal, A. *Chem. - Eur. J.* **2017**, *23*, 11611−11619.

(29) Zhou, Y.; Liu, B.; Sun, X.; Li, J.; Li, G.; Huo, Q.; Liu, Y. *Cryst. Growth Des.* **2017**, *17*, 6653−6659.

(30) Tothadi, S.; Desiraju, G. R. *Cryst. Growth Des.* **2012**, *12*, 6188−6198.

(31) Lai, H. W. H.; Wiscons, R. A.; Zentner, C. A.; Zeller, M.; Rowsell, J. L. C. *Cryst. Growth Des.* **2016**, *16*, 821−833.

(32) Nandi, S.; Chakraborty, D.; Vaidhyanathan, R. *Chem. Commun.* **2016**, *52*, 7249−7252.

(33) Rodríguez-Cuamatzi, P.; Luna-García, R.; Torres-Huerta, A.; Bernal-Uruchurtu, M. I.; Barba, V.; Höpfl, H. *Cryst. Growth Des.* **2009**, *9*, 1575−1583.

(34) van Megen, M.; Frank, W.; Reiss, G. J. *Z. Kristallogr. - Cryst. Mater.* **2015**, *230*, 485−494.

(35) Białek, M. J.; Zaręba, J. K.; Janczak, J.; Zoń, J. *Cryst. Growth Des.* **2013**, *13*, 4039−4050.
(36) Deng, Z.-P.; Huo, L.-H.; Zhao, H.; Gao, S. *Cryst. Growth Des.* **2012**, *12*, 3342−3355.
(37) Russell, V. A.; Evans, C. C.; Li, W.; Ward, M. D. *Science* **1997**, *276*, 575−579.
(38) Voogt, J. N.; Blanch, H. W. *Cryst. Growth Des.* **2005**, *5*, 1135−1144.
(39) Lemmerer, A.; Bourne, S. A.; Fernandes, M. A. *Cryst. Growth Des.* **2009**, *9*, 2265−2279.
(40) Xiao, W.; Hu, C.; Ward, M. D. *J. Am. Chem. Soc.* **2014**, *136*, 14200−14206.
(41) Li, Y.-N.; Huo, L.-H.; Deng, Z.-P.; Zou, X.; Zhu, Z.-B.; Zhao, H.; Gao, S. *Cryst. Growth Des.* **2014**, *14*, 2381−2393.
(42) Zhang, X.-L.; Ye, B.-H.; Chen, X.-M. *Cryst. Growth Des.* **2005**, *5*, 1609−1616.
(43) van Megen, M.; Frank, W.; Reiss, G. J. *CrystEngComm* **2016**, *18*, 3574−3584.
(44) Zon, J.; Videnova-Adrabinska, V.; Janczak, J.; Wilk, M.; Samoc, A.; Gancarz, R.; Samoc, M. *CrystEngComm* **2011**, *13*, 3474−3484.
(45) Shi, F.-N.; Trindade, T.; Rocha, J.; Paz, F. A. A. *Cryst. Growth Des.* **2008**, *8*, 3917−3920.
(46) Schütrumpf, A.; Kirpi, E.; Bulut, A.; Morel, F. L.; Ranocchiari, M.; Lork, E.; Zorlu, Y.; Grabowsky, S.; Yücesan, G.; Beckmann, J. *Cryst. Growth Des.* **2015**, *15*, 4925−4931.
(47) Hix, G. B.; Caignaert, V.; Rueff, J.; Le Pluart, L.; Warren, J. E.; Jaffrès, P.-A. *Cryst. Growth Des.* **2007**, *7*, 208−211.
(48) Kong, D.; Yao, J.; Clearfield, A.; Zon, J. *Cryst. Growth Des.* **2008**, *8*, 2892−2898.
(49) Jiménez-García, L.; Kaltbeitzel, A.; Enkelmann, V.; Gutmann, J. S.; Klapper, M.; Müllen, K. *Adv. Funct. Mater.* **2011**, *21*, 2216−2224.
(50) Zaręba, J. K.; Białek, M. J.; Janczak, J.; Zoń, J.; Dobosz, A. *Cryst. Growth Des.* **2014**, *14*, 6143−6153.
(51) Pietschnig, R.; Spirk, S. *Coord. Chem. Rev.* **2016**, *323*, 87−106.
(52) Chandrasekhar, V.; Boomishankar, R.; Nagendran, S. *Chem. Rev.* **2004**, *104*, 5847−5910.
(53) Pietschnig, R. *Main Group Strategies towards Functional Hybrid Materials*; Baumgartner, T., Jäkle, F., Eds.; John Wiley & Sons, Ltd: Chichester, UK, 2017.
(54) Suzuki, J.; Shimojima, A.; Fujimoto, Y.; Kuroda, K. *Chem. - Eur. J.* **2008**, *14*, 973−980.
(55) Prabusankar, G.; Murugavel, R.; Butcher, R. J. *Organometallics* **2004**, *23*, 2305−2314.
(56) Prabusankar, G.; Murugavel, R.; Butcher, R. J. *Organometallics* **2005**, *24*, 2124−2128.
(57) Hurkes, N. F.; Bruhn, C.; Belaj, F.; Pietschnig, R.; Krekić, K. *Z. Anorg. Allg. Chem.* **2016**, *642*, 302−305.
(58) Cerveau, G.; Corriu, R. J. P. J. P.; Dabiens, B.; Le Bideau, J. *Angew. Chem.* **2000**, *112*, 4707−4711.
(59) Cerveau, G.; Chappellet, S.; Corriu, R. J. P.; Dabiens, B.; Le Bideau, J. *Organometallics* **2002**, *21*, 1560−1564.
(60) Liu, M.; Tran, N. T.; Franz, A. K.; Lee, J. K. *J. Org. Chem.* **2011**, *76*, 7186−7194.
(61) Velásquez-Hernández, M. de J.; Torres-Huerta, A.; Hernández-Balderas, U.; Martínez-Otero, D.; Núñez-Pineda, A.; Jancik, V. *Polyhedron* **2017**, *122*, 161−171.
(62) Tran, N. T.; Wilson, S. O.; Franz, A. K. *Chem. Commun.* **2014**, *50*, 3738−3740.
(63) Benoit, R. L.; Lefebvre, D.; Fréchette, M. *Can. J. Chem.* **1987**, *65*, 996−1001.
(64) Vallat, A.; Meunier-Prest, R.; Laviron, E. *J. Electroanal. Chem.* **1997**, *428*, 11−17.
(65) Férey, G.; Serre, C. *Chem. Soc. Rev.* **2009**, *38*, 1380−1399.
(66) Tian, J.; Thallapally, P. K.; McGrail, B. P. *CrystEngComm* **2012**, *14*, 1909−1919.
(67) de Lange, M. F.; Verouden, K. J. F. M.; Vlugt, T. J. H.; Gascon, J.; Kapteijn, F. *Chem. Rev.* **2015**, *115*, 12205−12250.
(68) Rouquerol, F.; Rouquerol, J.; Sing, K. S. W.; Llewllyn, P.; Maurin, G. *Adsorption by Powders and Porous Solids; Principles, Methodology and Applications*; Elsevier Press, 2014.
(69) Ibarra, I. A.; Tan, K. E.; Lynch, V. M.; Humphrey, S. M. *Dalt. Trans.* **2012**, *41*, 3920−3923.
(70) Humphrey, S. M.; Chang, J.-S.; Jhung, S. H.; Yoon, J. W.; Wood, P. T. *Angew. Chem., Int. Ed.* **2007**, *46*, 272−275.
(71) Lee, J.; Waggoner, N. W.; Polanco, L.; You, G. R.; Lynch, V. M.; Kim, S. K.; Humphrey, S. M.; Sessler, J. L. *Chem. Commun.* **2016**, *52*, 8514−8517.
(72) López-Olvera, A.; Sánchez-González, E.; Campos-Reales-Pineda, A.; Aguilar-Granda, A.; Ibarra, I. A.; Rodríguez-Molina, B. *Inorg. Chem. Front.* **2017**, *4*, 56−64.
(73) Zhao, X. *Science* **2004**, *306*, 1012−1015.
(74) Choi, H. J.; Dincă, M.; Long, J. R. *J. Am. Chem. Soc.* **2008**, *130*, 7848−7850.
(75) Linder-Patton, O. M.; Bloch, W. M.; Coghlan, C. J.; Sumida, K.; Kitagawa, S.; Furukawa, S.; Doonan, C. J.; Sumby, C. J. *CrystEngComm* **2016**, *18*, 4172−4179.
(76) Sumida, K.; Rogow, D. L.; Mason, J. A.; McDonald, T. M.; Bloch, E. D.; Herm, Z. R.; Bae, T.-H.; Long, J. R. *Chem. Rev.* **2012**, *112*, 724−781.
(77) Chowdhury, F. A.; Yamada, H.; Higashii, T.; Goto, K.; Onoda, M. *Ind. Eng. Chem. Res.* **2013**, *52*, 8323−8331.
(78) Robinson, K.; McCluskey, A.; Attalla, M. I. *ChemPhysChem* **2012**, *13*, 2331−2341.
(79) Robinson, K.; McCluskey, A.; Attalla, M. I. *ChemPhysChem* **2011**, *12*, 1088−1099.
(80) Ibarra, I. A.; Lin, X.; Yang, S.; Blake, A. J.; Walker, G. S.; Barnett, S. A.; Allan, D. R.; Champness, N. R.; Hubberstey, P.; Schröder, M. *Chem. - Eur. J.* **2010**, *16*, 13671−13679.
(81) Dizman, B.; Elasri, M. O.; Mathias, L. J. *J. Appl. Polym. Sci.* **2004**, *94*, 635−642.
(82) Sneh, O.; George, S. M. *J. Phys. Chem.* **1995**, *99*, 4639−4647.
(83) *SAINT; SADABS*; Bruker AXS Inc.: Madison, Wisconsin, USA, 2007.
(84) Sheldrick, G. M. *Acta Crystallogr., Sect. A: Found. Adv.* **2015**, *71*, 3−8.
(85) Sheldrick, G. M. *Acta Crystallogr., Sect. C: Struct. Chem.* **2015**, *71*, 3−8.
(86) Hübschle, C. B.; Sheldrick, G. M.; Dittrich, B. *J. Appl. Crystallogr.* **2011**, *44*, 1281−1284.
(87) CrystalMaker Software Ltd, Oxford, England, http://www.crystalmaker.com.
(88) Mercury CSD 3.9 Software, http://www.ccdc.cam.ac.uk/mercury/.
(89) GIMP 2.8: The GNU Image Manipulation Program, http://www.gimp.org.

DOI: 10.1021/acs.cgd.8b00030
Cryst. Growth Des. 2018, 18, 3805−3819